

CHAPTER 6

SETUP FOR THE EXPERIMENTAL STUDY

6.1 Introduction

Researches in the theoretical development and the experimental study of structural damage diagnosis have been vigorously expanded during last two decades. Most objects of interest for analysis or experiment, however, were limited to simple structures [1, 103-107], small-sized models or specimens [44, 108-110], or bridge structures [16, 111-116]. In the past years, despite Yao and his co-workers [28], Elkordy and his colleagues [61], and ASCE Structural Health Monitoring Committee [117], not too many researchers devoted themselves to the experiment investigation of the damage diagnosis in large-scaled building structures. As we know, the damage diagnosis for real-world civil structures is very difficult. Due to the inherent inconsistency between the model and real structure (especially when the size of the structure becomes larger), when the developed theories for the structural damage diagnosis were applied to practical cases, the results may not be as good as we expect, even though the theoretical analysis and the numerical results were perfect. Nevertheless, this work aims to investigate and exam the proposed methods through the conducted experiments to provide a full looks on the study of the structural health monitoring. Consequently, the author designs a scaled-down four-story steel frame to perform the experimental study in this dissertation. The conducted experiments aim to

investigate the following topics.

- (1) To verify the proposed ANN-based system identification model or approach.

The ANNSI model and the monitoring networks are applied to the experimental data, which are generated in various simulated damage scenarios, to verify if the changes in system characteristics can be identified. The ANNSI model is used to identify the modal parameters of the specimen from the acceleration as well as the strain measurements. The modal parameters obtained from two types of measurements provide basis for diagnosing the condition of the structure. In addition, the monitoring networks are also trained by the acceleration and strain measurements to be used for identifying the structure.

- (2) To verify the proposed damage detection/diagnosis strategies.

By using the structural modal parameters obtained from the SI models, the damage site is first located by the UFN model and the damage extent is then estimated. In addition, the trained system monitoring networks, such global monitoring networks and decentralized monitoring networks are applied to monitor the test frame in different damage scenarios.

- (3) To investigate the capabilities of the fiber Bragg grating sensors for structure monitoring.

Since the fiber Bragg grating (FBG) sensors were first demonstrated for strain and temperature measurement, they have been subject to continuous and rapid development. The main reason for this is because the FBG sensors have a number of distinguishing advantages which will be pointed out later

in Section 6.3. According to the distinguishing advantages of the FBG sensors, they seem to be ideal for realizing so-called ‘fiber-optic smart structures’ where the FBG sensors were installed to the structure for health monitoring via the provision of real-time sensing information, such as strain, temperature, and vibration. In this work, consequently, several FBG sensors were attached to the experimental specimen as the ‘structural nerves’ to monitor the structure. In addition to the FBG sensors, several electrical strain gages were also adhered beside the FBG sensors to the specimen for comparison.

- (4) To explore the possibility of other damage related indicators.

The DLF and network prediction error are used as damage indicators for detecting the structural damage. Some other potential indicators will be also explored and discussed by directly using the experimental measurements obtained in the shaking table tests.

- (5) To provide a reference for the experiment investigation of the damage diagnosis of large-scaled building structures.

Besides the preparing integrated project of NCSD, ‘Researches on structural health monitoring and structural control: experimental verification of large-scaled benchmark model’, few researchers in Taiwan engaged in the experiment of the structural damage detection or health monitoring, recently. The study in structural damage detection and health monitoring has received more and more attention in recent year. Since the damage detection of practical structures remains a difficult and challenging task, the author hope to present a preliminary study on this topic as a reference.

Subsequently, the characterizations of the experimental specimen, the organization of the measuring instruments, the design of the simulated structural deterioration, the experiment layouts, and the preliminary analysis on the observed measurements are consecutively introduced in the following sections.

6.2 Shaking Table And Experimental Specimen

The damage detection approaches demonstrated in Chapter 5 is going to be further verified in this work by the experimental data. For this reason, a series of shaking table tests of a steel frame structure for health monitoring study was conducted in the laboratory in the department of civil engineering, National Chiao Tung University (NCTU).



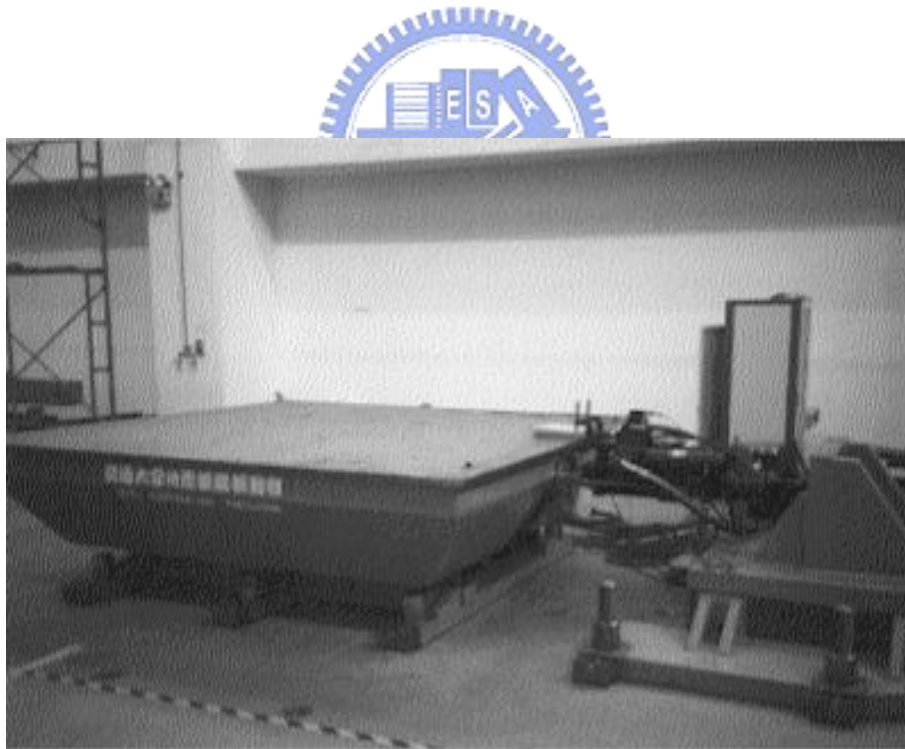
6.2.1 The Shaking Table In NCTU

Table 6.1 depicts the basic description of the shaking table (or earthquake emulator) in NCTU. Figure 6.1 shows the appearance of the shaking table. This shaking table is a 3m long, 3m wide, and 5 tons uni-axial earthquake simulator. The maximum weight capacity of the experimental specimen for this table to carry is about 10 tons. The shaking table can simulated any earthquake in the world to the intensity of ± 1 g.

The Kobe earthquake, of which the intensity is reduced to 0.08g, is used as the input excitations to the shaking table throughout the experiments. Figure 6.2 shows the time-history and spectrum of the input excitation (Kobe earthquake with PGA 0.08g).

Table 6.1 Specifications of the shaking table in NCTU

| Item | Value |
|-------------------------------|------------|
| Table size (m^2) | 3×3 |
| Weight of table (kg) | 5000 |
| Max. specimen weight (kg) | 10,000 |
| Max. displacement (cm) | ± 12.5 |
| Max. velocity (cm/sec) | ± 60 |
| Max. acceleration (g) | ± 1 |

**Figure 6.1** Earthquake simulator- the shaking table system in NCTU

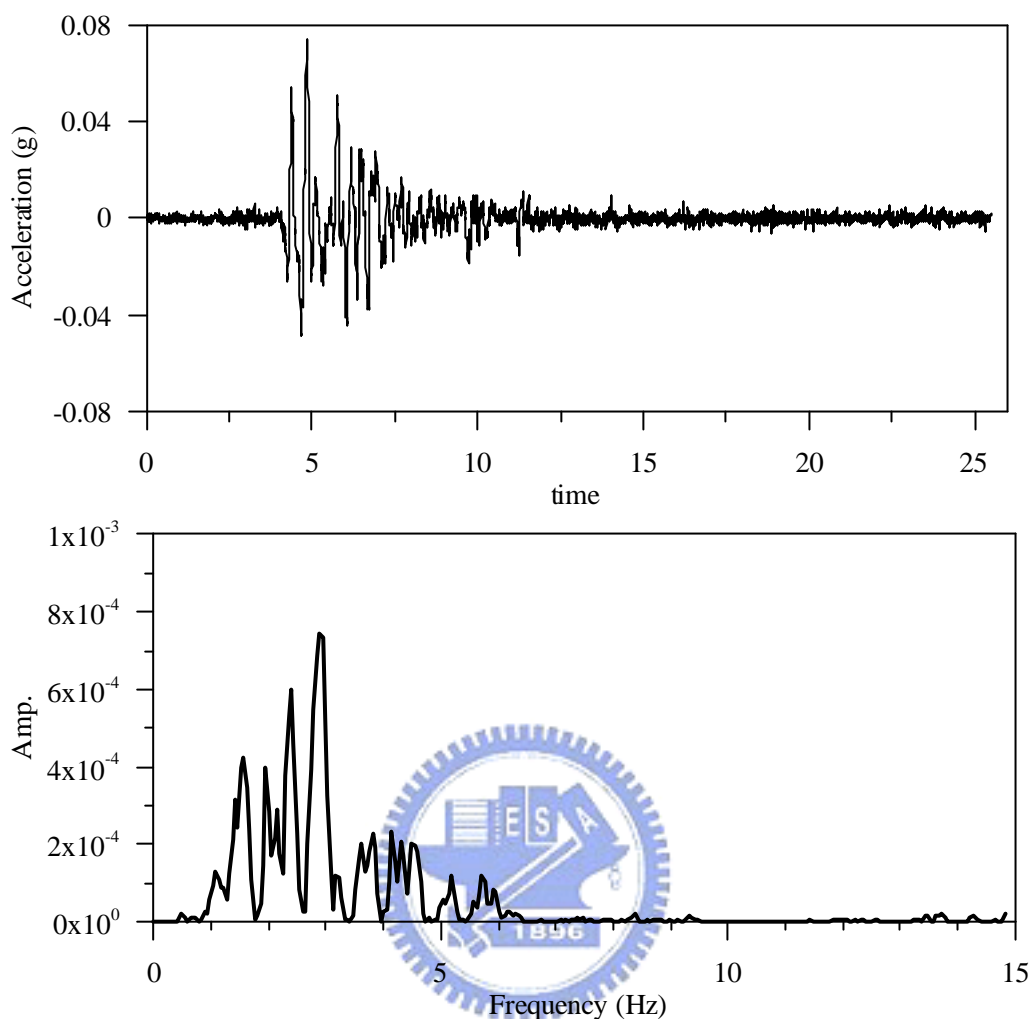


Figure 6.2 Time-history and frequency spectrum of the 0.08g Kobe earthquake

6.2.2 Four-Story Steel Test Model

A four-story steel frame was designed and constructed to perform the experiments. The four-story test model is a 2m long, 2m wide, and 6.4m high steel frame. Lead blocks were piled on each floor such that the mass of each floor was approximately $120 \text{ kg} - \text{s}^2 / \text{m}$. The experimental specimen is designed to be a ‘soft structure’ for the sake of obtaining the modal parameters easily and explicitly. Figure 6.3 diagrams the four-story frame. The characterizations of the experimental specimen are listed in

Table 6.2. The detailed cross sections of the members are shown in Figure 6.4.

According to the parameters listed in Table 6.2, an analytical model was established and analyzed via the ETABS software. Table 6.3 shows the modal parameters of the analytical model. Note that, because the experiments were designed to execute along the transverse direction (i.e. y -axis), Table 6.3 only shows the modal parameters of the model along the y -axis.

Table 6.2 The characterizations of the experimental specimen

| Item | Value |
|--------------------------------------|-----------------------------------|
| Plane size (m^2) | 2×2 |
| Story height (m) | 1.6 |
| Weight (kg) | ≈ 5000 |
| Cross section of the column (mm) | $125 \times 60 \times 6 \times 8$ |
| Cross section of the beam (mm) | $125 \times 60 \times 6 \times 8$ |
| Cross section of the girder (mm) | $100 \times 50 \times 5 \times 7$ |
| Size of the mass block (mm) | $1360 \times 1360 \times 32$ |
| Mass at 4th floor ($kg - s^2 / m$) | 117.06 |
| Mass at 3rd floor ($kg - s^2 / m$) | 121.21 |
| Mass at 2nd floor ($kg - s^2 / m$) | 121.21 |
| Mass at 1st floor ($kg - s^2 / m$) | 121.54 |

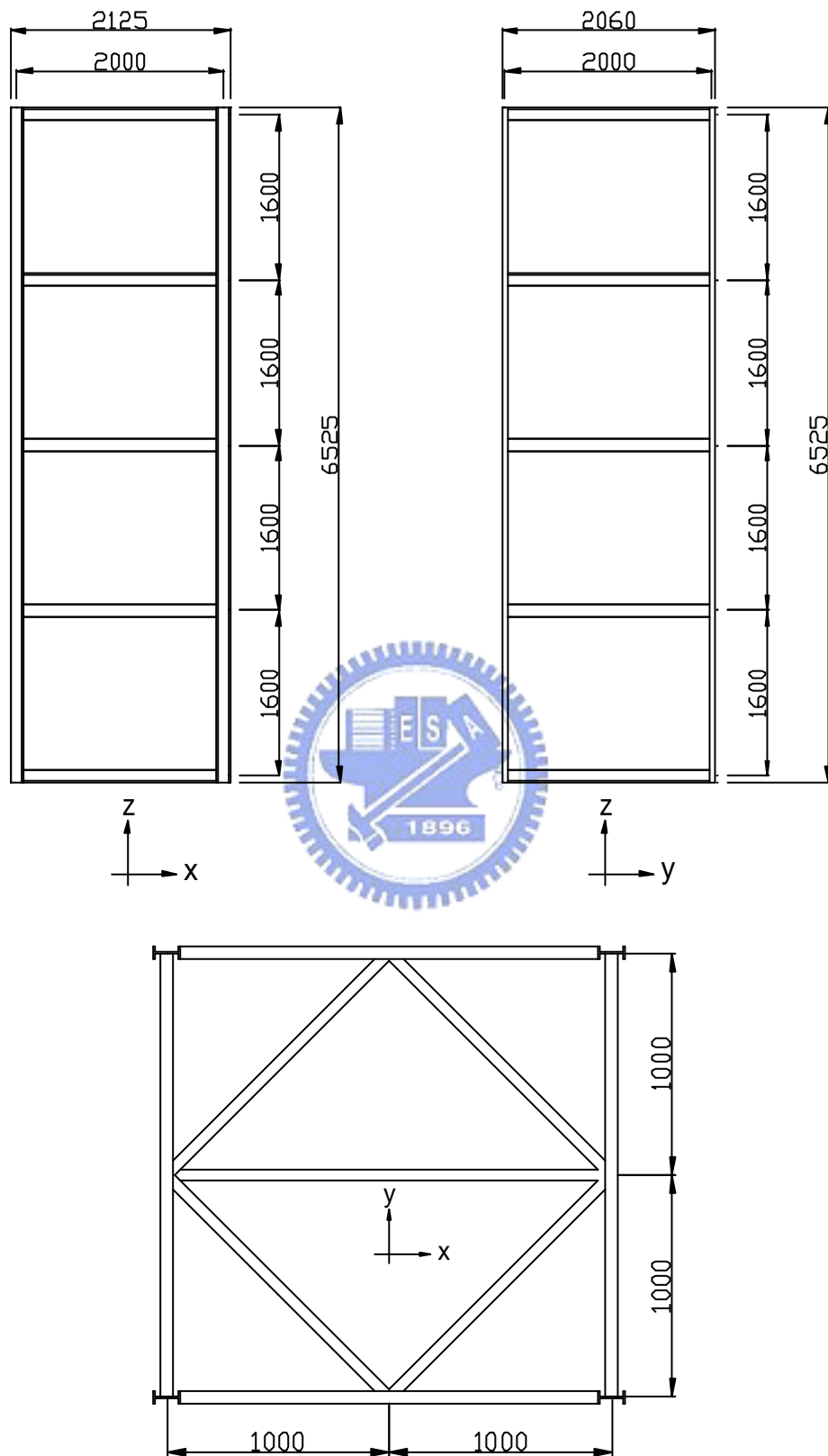


Figure 6.3 Schematic diagrams of the four-story frame (unit: mm)

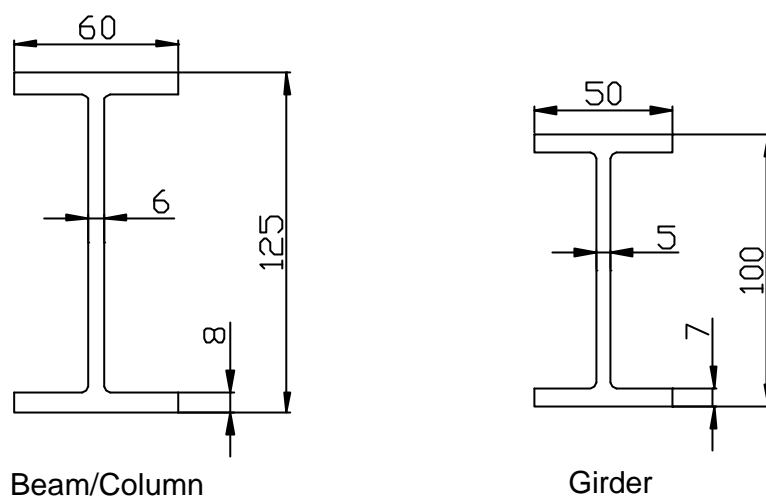


Figure 6.4 Member cross section of the test model (unit: mm)

Table 6.3 Analytical modal parameters of the test model in the transverse direction

| <i>Mode</i> | 1 | 2 | 3 | 4 | |
|--------------------------|-----------|----------|----------|----------|--------|
| <i>Frequency (Hz)</i> | 1.18 | 3.48 | 5.45 | 6.80 | |
| <i>Damping ratio (%)</i> | 5 | 5 | 5 | 5 | |
| <i>Mode shape</i> | 4F | 1.000 | 1.000 | 0.664 | 0.380 |
| | 3F | 0.879 | 0.011 | -0.846 | -0.903 |
| | 2F | 0.648 | -0.998 | -0.348 | 1.000 |
| | 1F | 0.332 | -0.976 | 1.000 | -0.659 |

Figure 6.5 shows the photo of the four-story steel frame after locked on the shaking table. The author would like to mention that, the steel frame shown in this photo which was constructed by the columns, beams, girders, and mass blocks but not installed with ‘strengthening column’ is termed as ‘clear frame’. The description about the strengthening column will be expanded later in Section 6.4.



Figure 6.5 A photo of the four-story clear frame

6.3 Sensing Instrumentations

Three types of sensors, including accelerometers, electrical resistance strain gages (RSG), and optic fiber Bragg grating (FBG) sensors, were installed on the specimen to measure the structural responses during the shaking table tests. The basic information, such as the specifications and arrangements of the sensors, about the sensing instrumentations is briefly introduced in the followings.

6.3.1 Accelerometers

Five accelerometers were designed to monitor the acceleration responses of the test specimen when subjected to the simulated earthquakes. Figure 6.6 shows the deployment of the accelerometers. According to the figure, four accelerometers were placed along the central line of the frame at each floor to measure the structural responses, and one accelerometer was placed at the foot of the column to measure the input base excitation to the structure. Figure 6.7 and 6.8 show the actual installations of the accelerometers at the 2nd floor and base, respectively. A simple description of the employed accelerometers is listed in Table 6.4 in which the symbols A1 to A4 represent the accelerometers at the 1st to 4th floor, respectively, and the symbol Abase represents the accelerometer at the base.



Table 6.4 Specifications of the accelerometers

| | TYPE | Axes | Span (g) |
|--------------|--------------------------|------|----------|
| A4 | <i>CrossBow</i> CXL02LF1 | X | ± 2 |
| A3 | <i>CrossBow</i> CXL02LF1 | X | ± 2 |
| A2 | <i>CrossBow</i> CXL01LF1 | X | ± 1 |
| A1 | <i>CrossBow</i> CXL01LF1 | X | ± 1 |
| Abase | <i>CrossBow</i> CXL01LF1 | X | ± 1 |

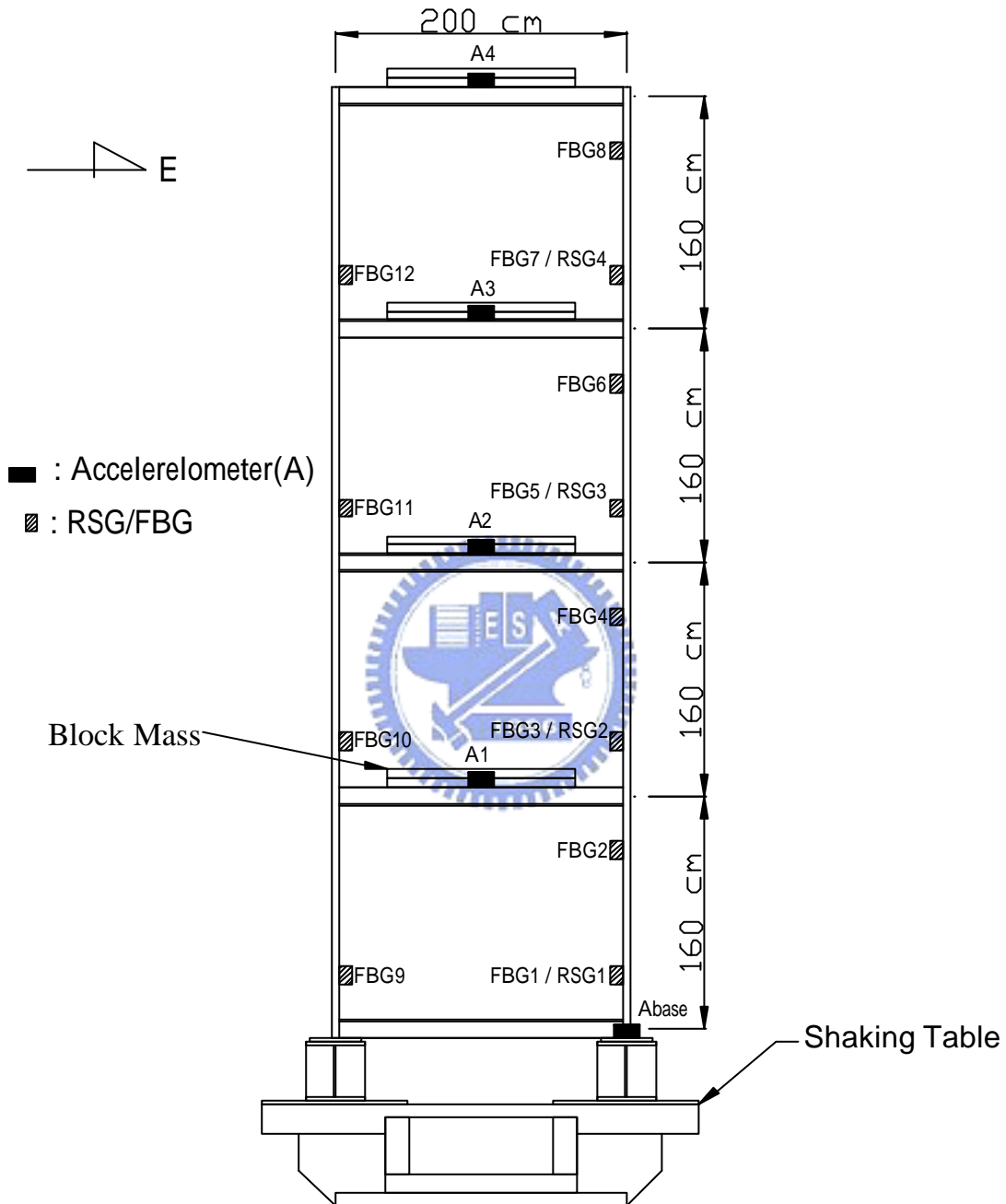


Figure 6.6 Displacement of the sensing instrumentations



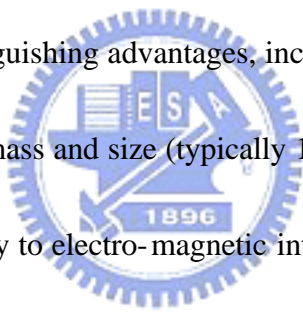
Figure 6.7 Accelerometer at the 2nd floor of the test frame



Figure 6.8 Accelerometer at the base of the test frame

6.3.2 FBG sensors And RSGs

Fiber Bragg grating sensors are one of the most exciting developments in the field of optical fiber sensors in recent years. Since the pioneering work done by Meltz *et al.* [118], subsequent interest in FBG sensors has increased considerably. One of the probable main reasons for this is that, FBG sensors have great potential for a wide range of sensing applications for important physical quantities, such as strain, temperature, pressure, acceleration [119-121], etc. In this work, the FBG sensors are used for measuring the strain responses of the structure during earthquakes. FBG sensors have a number of distinguishing advantages which make them a promising candidate for smart structures. When compared with RSG used for strain monitoring, FBG sensors have several distinguishing advantages, including [122]

- 
- (1) much less intrusive mass and size (typically 125 μm in diameter);
 - (2) much better immunity to electro-magnetic interference;
 - (3) greater capacity of multiplexing a large number of sensors along a single fiber link, unlike RSGs which need a huge amount of wiring;
 - (4) greater resistance to corrosion when used in structures, such as bridges and dams;
 - (5) higher temperature capacity (typically about 300 $^{\circ}\text{C}$);
 - (6) longer lifetime for long term operation.

These features have made FBG sensor very attractive for health monitoring of smart structures.

Sensing principle of FBG sensor

An FBG is written into a segment of Ge-doped single mode fiber in which a periodic modulation of the core refractive index is formed by exposure to a spatial pattern of ultraviolet light in the region of 244-248 nm. The lengths of FBG sensors are normally within the region of 1-20mm and grating reflectivities can approach ~100%. Being a recent developed technique for civil engineering, the sensing principle of FBG sensor is briefly introduced herein. When the FBG is illuminated by a broadband light source, each FBG sensor in a fiber reflects a specific wavelength that shifts slightly depending on the strain applied to the sensor. The change in wavelength is directly proportional to the change in mechanical features such as strain or temperature.

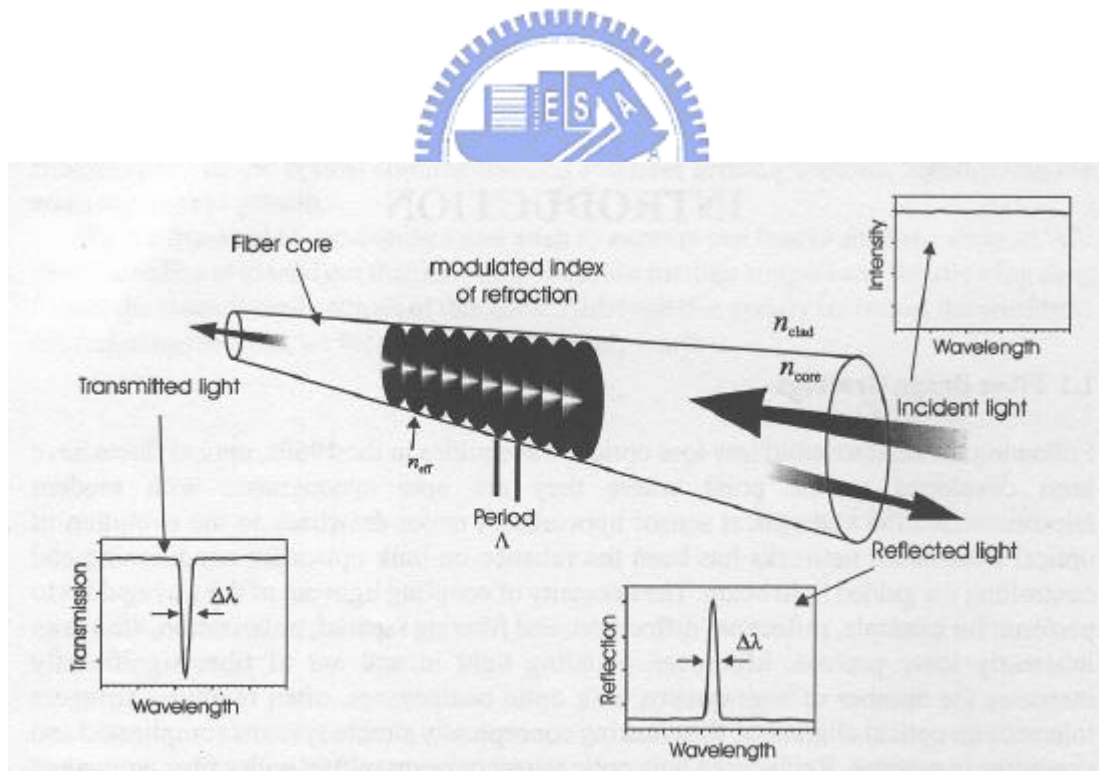


Figure 6.9 A schematic representation of a fiber Bragg grating

(extracted from Othonos and Kalli, 1999 [123])

In its simplest form a fiber Bragg grating consists of a periodic modulation of the refractive index in the core of a single-mode optical fiber (Figure 6.9). According to Bragg's law, reflected Bragg wavelength, λ_B , is given by

$$\lambda_B = 2n_{\text{eff}} \Lambda \quad (6.1)$$

where n_{eff} represents the effective refractive index of the fiber core and Λ is the period of the index modulation.

The Bragg wavelength is the free space center wavelength of the input light that will be back-reflected from the Bragg grating. The Bragg grating resonance, which is the center wavelength of reflected light from a Bragg grating, depends on the effective index of refraction of the core and the periodicity of the grating. The effective index of refraction, as well as the periodic spacing between the grating planes, will be affected by changes in strain and temperature. While the strain effect, which corresponds to a change in the grating spacing and the strain-optic induced change in the refractive index, is considered (Figure 6.10), the Bragg wavelength change can be expressed as

$$\Delta \lambda_B = 2n_{\text{eff}}^* \Delta \Lambda \quad (6.2)$$

where n_{eff}^* is the changed effective refractive index. Hence the wavelength shift,

$\frac{\Delta \lambda_B}{\lambda_B}$, can be derived.

$$\frac{\Delta \lambda_B}{\lambda_B} = \frac{2n_{\text{eff}}^* \Delta \Lambda}{2n_{\text{eff}} \Lambda} = \frac{n_{\text{eff}}^*}{n_{\text{eff}}} \frac{\Delta \Lambda}{\Lambda} = k_e \frac{\Delta l}{l} = k_e \epsilon \quad (6.3)$$

where k_e is a strain-sensitive coefficient. Furthermore, the Bragg wavelength shift due to the temperature effect may be written as

$$\frac{\Delta I_B}{I_B} = (\mathbf{x} + \mathbf{a})\Delta T = \mathbf{k}_T \Delta T \quad (6.4)$$

where ΔT is the change in temperature; \mathbf{x} is the thermal optical coefficient; \mathbf{a} is the thermal expansion coefficient; and \mathbf{k}_T represents the thermal-sensitive coefficient. Combining equations (6.3) with (6.4), the Bragg wavelength shift due to strain and thermal effects can be expressed as

$$\frac{\Delta I_B}{I_B} = \mathbf{k}_e \mathbf{e} + \mathbf{k}_T \Delta T \quad (6.5)$$

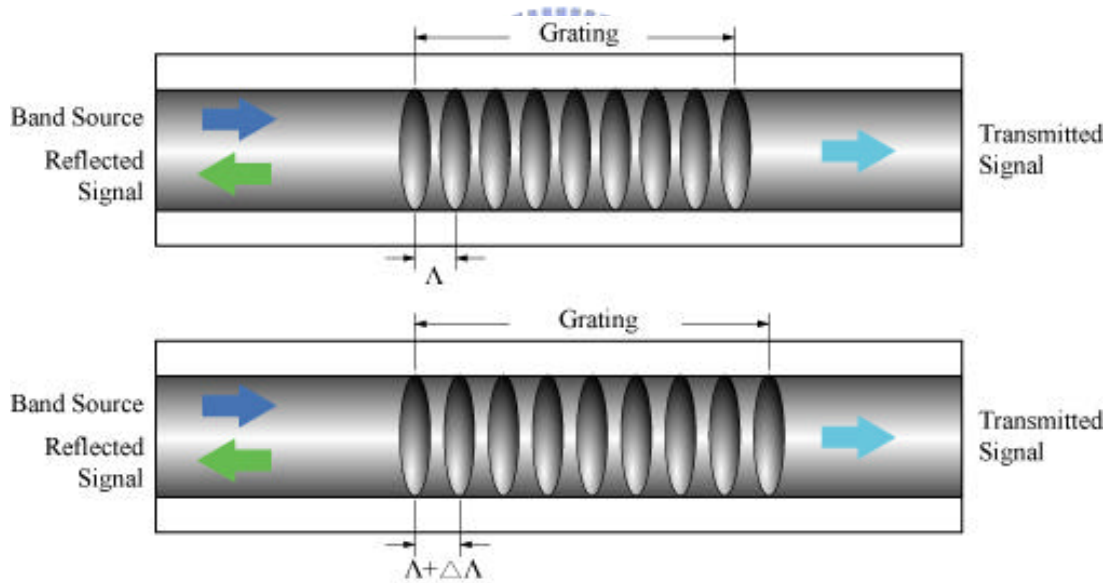


Figure 6.10 Illustration of a fiber Bragg grating with strain effect

Further details about the FBG sensor technology and its applications can be found in related books or review articles, such as Othonos and Kalli [123], Kashyap [124], and Rao [122, 125].

According to the experiments the strain-sensitive and thermal-sensitive coefficients provided by the Prime Optical Fiber Corporation (POFC, Hsinchu, Taiwan) are about 0.80 and 5.88×10^{-6} , respectively, which make equation (6.5) becomes

$$\frac{\Delta I_B}{I_B} = 0.80\epsilon + 5.88 \times 10^{-6} \Delta T \quad (6.6)$$

Then the strain or temperature variation can be converted from the wavelength change by the following relationship.

$$1\text{pm} \approx 0.8\text{mstrain} \approx 0.1^\circ\text{C} \quad (6.7)$$

FBG Data Acquisition System

An FBG data acquisition system, including the MOI's (Micron Optics, Inc.) Fiber Bragg Grating Swept Laser Interrogator (FBG-SLI) and a notebook (Figure 6.11), is adopted to monitor and restore the FBG wavelength data.

The FBG-SLI is a high-power, fast, multi-sensor measurement system that provides a major advancement for mechanical sensing applications. The FBG-SLI combines the speed of MOI's unique Swept Laser technology and the accuracy of the patented picoWave reference technique to resolve changes in optical wavelengths of approximately 1pm ($<1\text{ m strain}$) and achieve high calibrated wavelength accuracy. It is a complete system that includes a swept source used to illuminate the FBG sensors and the four detectors, which simultaneously measure the reflected optical signals on each fiber. All sensors (maximum of 64 FBG sensors per fiber) on all channels are scanned simultaneously at a maximum rate of 108Hz. Table 6.5 lists the specification of the FBG-SLI.



Figure 6.11 FBG data acquisition system

Table 6.5 Specifications of the FBG-SLI

| Optical | |
|--|---|
| Number of Optical Channels | 4 |
| Maximum Number of FBG Sensors/Channel | 64 (256 total across 4 channels) |
| Wavelength Range | 1525 - 1565 nm |
| Absolute Accuracy | +/- 5 pm (~4.2 $\mu\epsilon$) typ, +/- 10 pm max |
| Repeatability | +/- 2 pm (~1.7 $\mu\epsilon$) typ, +/- 5 pm max |
| Optical Power/Channel | -10 dBm approx. |
| Dynamic Range (4 software-controlled gain settings) | 30 dB |
| Resolution | <1 pm (~0.8 $\mu\epsilon$) |
| Scan Frequency | 108 Hz max |
| Minimum FBG Spacing | 0.5 nm |
| Optical Connector | FC/APC |
| Hardware and Software | |
| Computer Interface Card PCI or PC CARD | (PCMCIA) |
| Interface Cable | Included |
| FBG-IS Software for Windows 95, 98, 2000, NT and XP | Included |
| Electrical | |
| Power Supply | 95-135 VAC or 190-265 VAC, 15W |
| Uncalibrated Analog Output - BNC Connectors | Test, sync and scan |
| Mechanical | |
| Operating Temperature | 10° – 40°C |
| Dimensions | 69 x 277 x 267 mm |
| Weight | 4.1 kg |
| Options | |
| Test Processor | Laptop computer/data management system |
| Custom Optical Connectors | FC/SPC |
| Custom Computer Interface Cards | ISA |

A block diagram of the optical layout is shown in Figure 6.12. The swept laser illuminates the Bragg gratings and each FBG sensor reflects its corresponding wavelength. The Fiber Fabry-Perot Tunable Filter (FFP-TF) simultaneously scans the reflected wavelengths from the FBG sensors and the picoWave reference. Through the detector circuitry and software, the detected signals are converted to wavelengths. A PC or notebook provides the on-line calibration, data display/storage, and the FBG sensors under test.

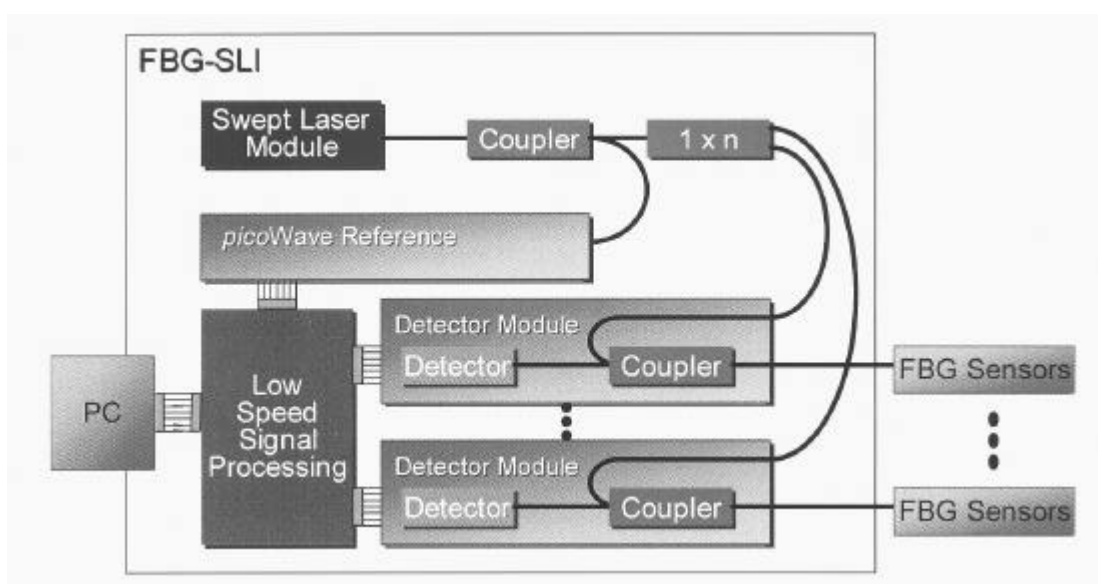


Figure 6.12 Block diagram of the optical layout (extracted from *FBG-SLI Instruction Manual, Version 4.0*)

FBG sensors arrangement

There are 12 FBG sensors along two fibers were employed in this work to monitor the strain responses of the test frame during excitations. Eight FBG sensors

were arranged along one fiber link which was connected to the first channel (terms as Channel 1) of the FBG-SLI, and four FBG sensors were arranged along another fiber link which was connected to the second channel (terms as Channel 2) of the FBG-SLI. The descriptions of the specification and arrangement of the FBG sensors along Channel 1 and Channel 2 are shown in Tables 6.6 and 6.7 and Figure 6.13, respectively. Figures 6.14 and 6.15 display the transmission and reflection spectra of the FBG sensors on Channel 1 and Channel 2, respectively.

The FBG sensors were attached to the columns at each story to measure the strain responses of the test frame. The FBG sensors along Channel 1 were located near the top and the bottom of the story columns on east side; meanwhile, the FBG sensors along Channel 2 were located near the bottom of the story columns on west side. A sketch of the deployment of the FBG sensors is also demonstrated in Figure 6.5. The actual attachments of FBG1 and FBG2 on Channel 1 and FBG9 on Channel 2 are shown in Figure 6.16, Figure 6.17, and Figure 6.18, respectively. Note that, FBG1 and RSG1 in Figure 6.16 were installed near the bottom of the column of 1st story on east side, FBG2 in Figure 6.17 was installed near the top of the column of 1st story on east side, and FBG9 in Figure 6.18 was installed near the bottom of the column of 1st story on west side.

In addition to the FBG sensors, four RSGs were also adopted as a reference to the FBG sensors. Therefore, one RSG was attached right beside the FBG sensor to the bottom of the column of each story, as shown in Figure 6.16. The RSGs configuration was also depicted in Figure 6.6.

Table 6.6 Center wavelength of the FBG sensors along Channel 1

| | FBG1 | FBG2 | FBG3 | FBG4 | FBG5 | FBG6 | FBG7 | FBG8 |
|------------------------|-------------|-------------|-------------|-------------|-------------|-------------|-------------|-------------|
| Wavelength (nm) | 1542 | 1545 | 1548 | 1551 | 1554 | 1557 | 1560 | 1563 |

Table 6.7 Center wavelength of the FBG sensors along Channel 2

| | FBG9 | FBG10 | FBG11 | FBG12 |
|------------------------|-------------|--------------|--------------|--------------|
| Wavelength (nm) | 1530 | 1533 | 1539 | 1536 |

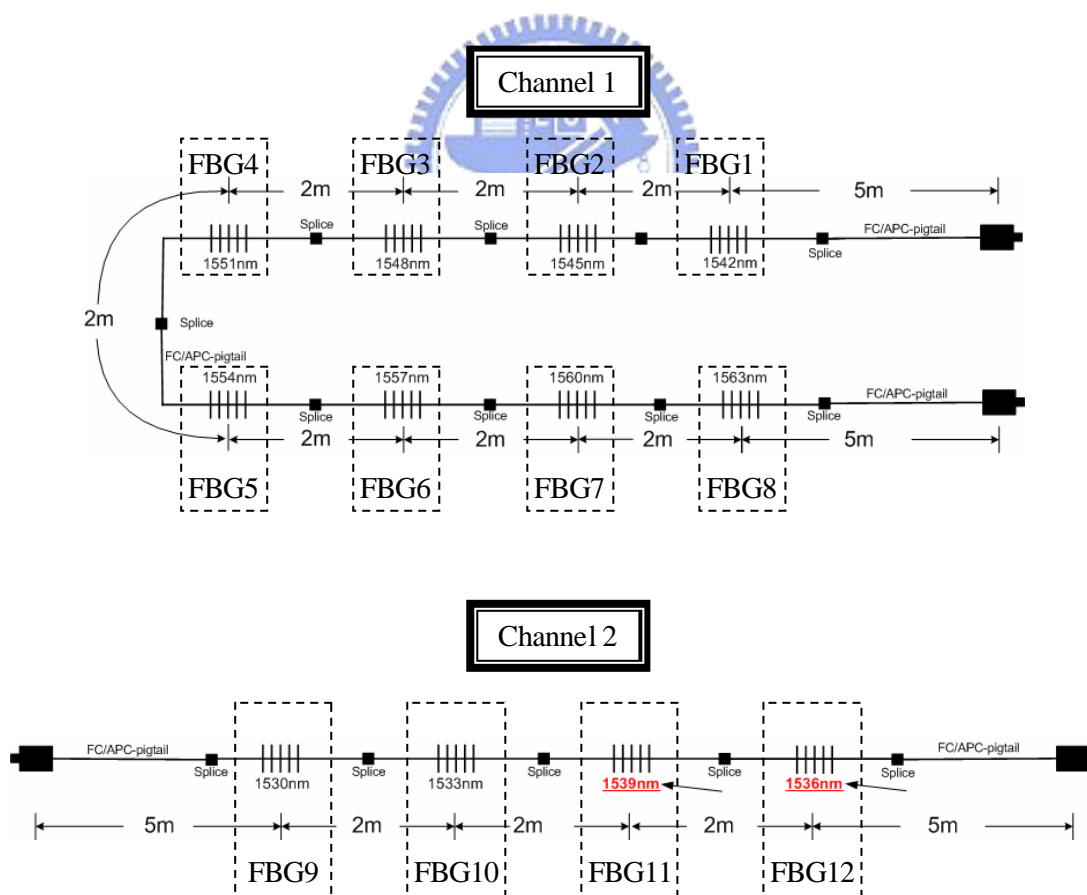


Figure 6.13 Configurations of the FBG sensors

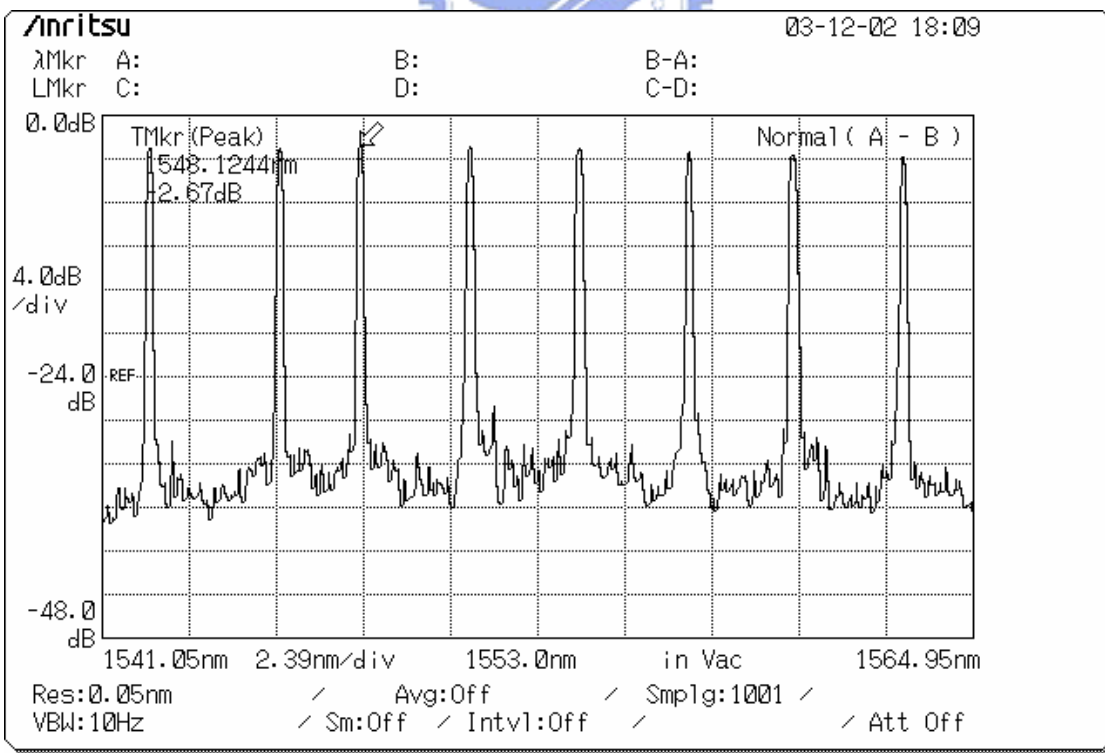
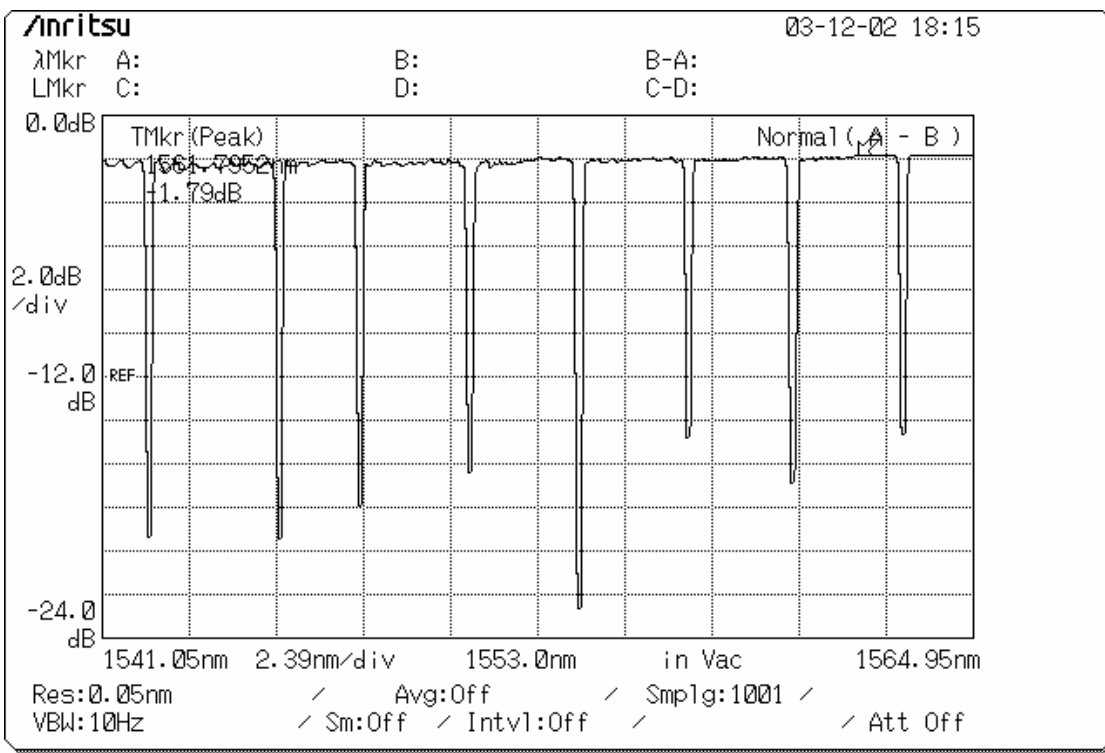


Figure 6.14 Transmission and reflection spectra of Channel 1 (POFC provided)

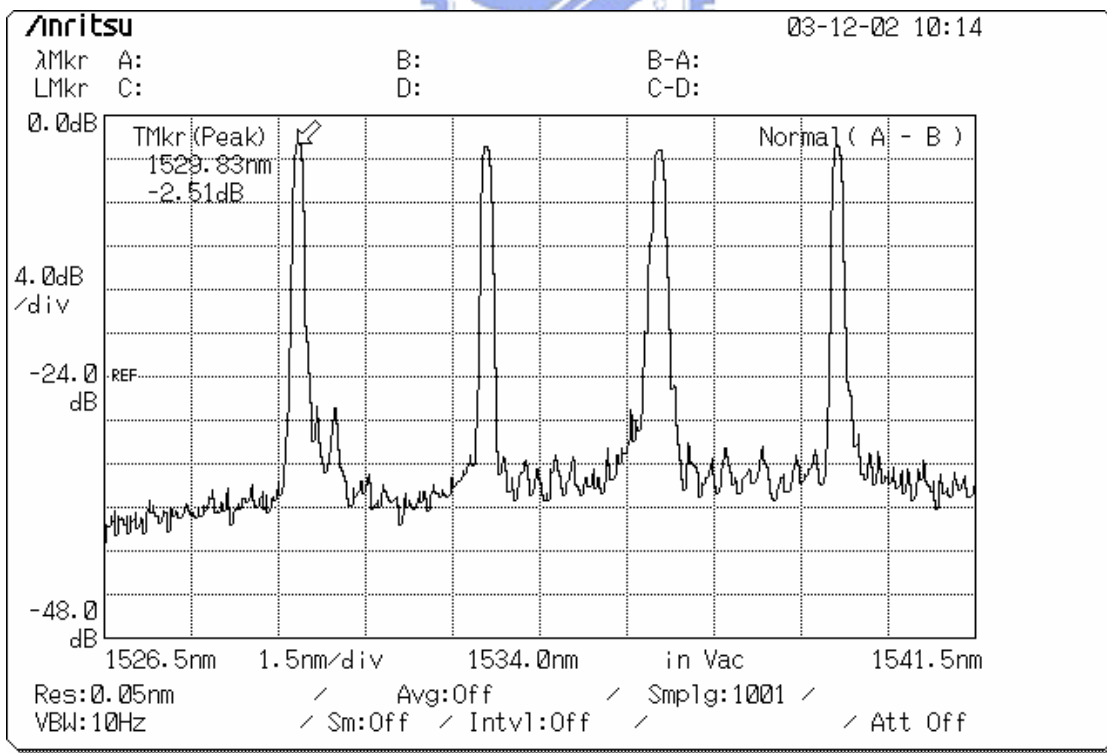
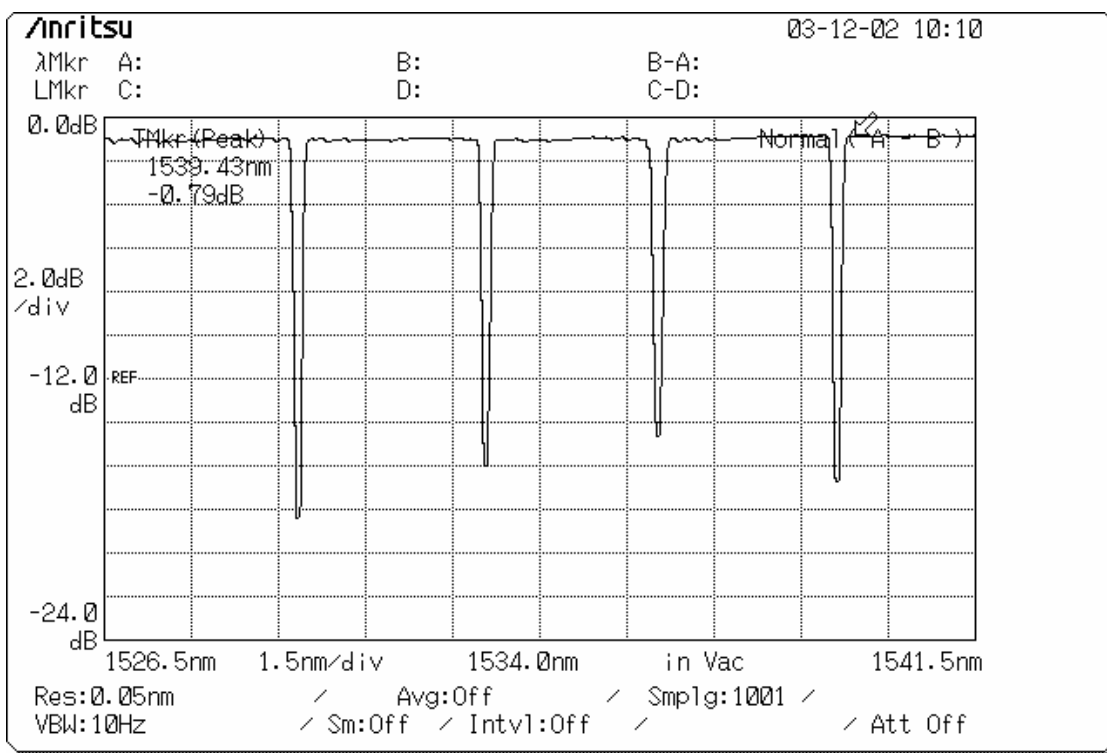


Figure 6.15 Transmission and reflection spectra of Channel 2 (POFC provided)

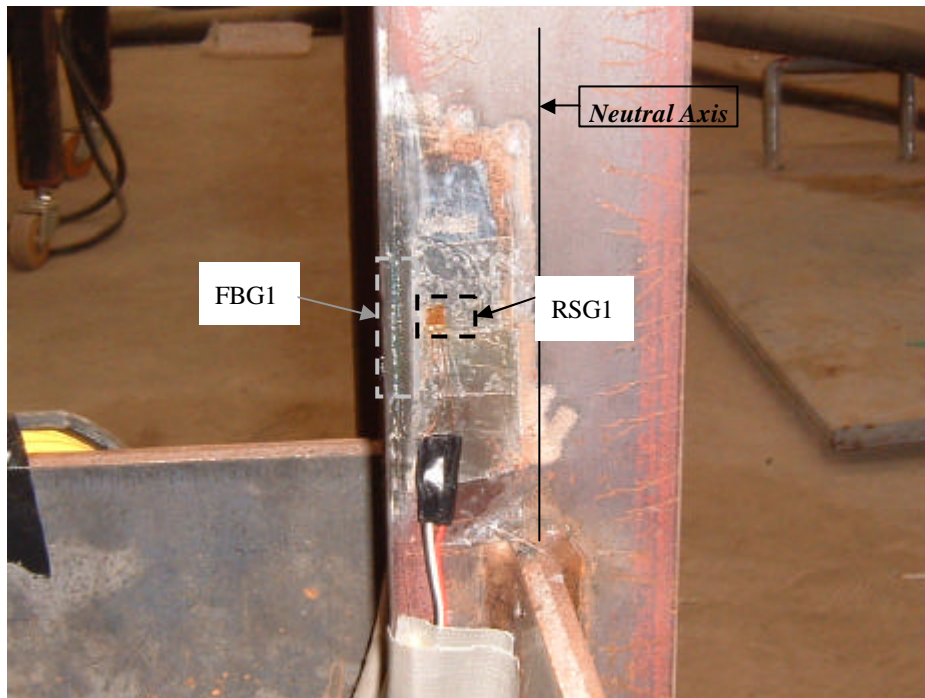


Figure 6.16 Locations of the FBG1 and RSG1

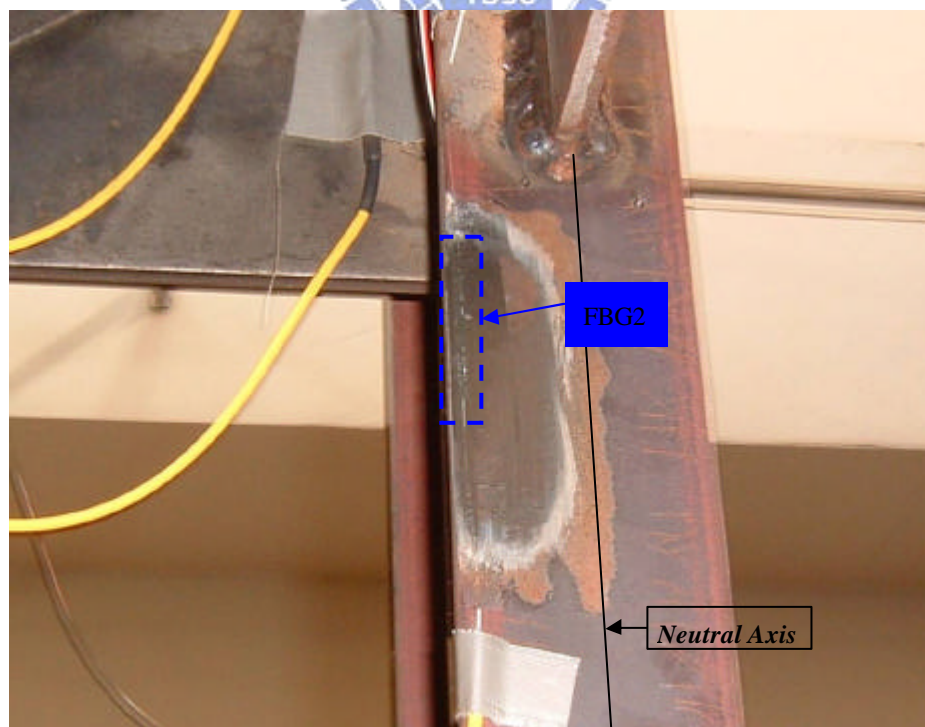


Figure 6.17 Location of the FBG2

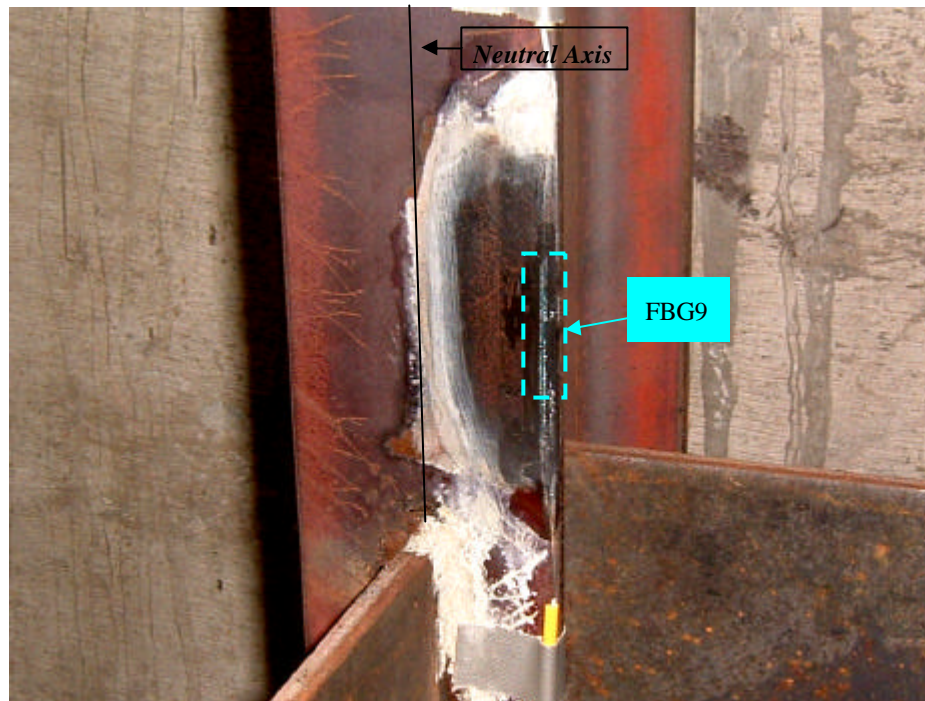


Figure 6.18 Location of the FBG9

6.4 Deteration Simulation

There are several kinds of mechanisms for deterioration simulation according to the study objectives of interest. By reviewing the numerical or experimental studies in damage detection or assessment during these years, the simulations of structural damage are classified into the following categories.

- (1) For beams-like or bridge structures:

decreasing the stiffness of the elements numerically [7];

reducing the thickness or cross-section of the selected elements [6, 68, 105, 113, 126-128];

support failure and/or crack degradation [29, 103, 111, 129].

(2) For truss structures:

reducing the cross-section or Young's modulus of the bars to simulate the axial stiffness failures [6, 25, 130];

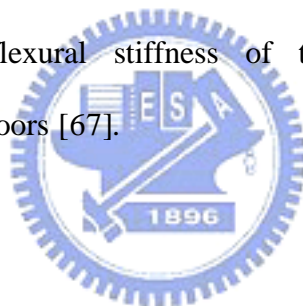
loss of stiffness and mass of members [27].

(3) For building or frame structures:

loosing the beam-column joints to simulate joints failures [24, 71];

weakening the story stiffness via the reduction in bracing areas [61];

reducing the flexural stiffness of the beams belonging to the corresponding floors [67].



6.4.1 Strengthening Column

The deterioration in a structure is assumed in this work to be the change in story stiffness. In most experimental studies of damage detection which is based on such an assumption commonly used bracing elements as simulations [61]. This work, however, employs a different type of mechanism, called the 'strengthening column (SC for short)', as simulations to the structural deterioration.

Most of the past experimental studies focus on high-level damage extent, and most of the successful diagnoses were usually based on the high-level damage. Small extent damage is not as easy and evident as large extent damage to be identified and assessed because of many uncertainties and errors such as boundary conditions,

measurement errors, ambient noise, and computation errors. Even though, this work attempts to investigate that if the small extent (or low-level) deterioration as well as the large extent (high-level) deterioration can be successfully identified and diagnosed.

Compare with the experimental specimens in the works conducted by Elkordy [61] and Koh [44], the specimen in this work is heavier and bigger. Furthermore, according to the analysis result from ETABS software, even small cross-section of bracing can provide significant lateral stiffness which results in considerable changes in the natural frequencies of the structure. In order to investigate whether small deterioration in a structure can be detected and assessed, simulation on small deterioration scenario is also considered in this work. Consequently, instead of using the bracing, the SC is designed to provide the specimen with additional lateral stiffness. The element selected to perform as SC is the lightweight 'C' shape steel. Table 6.8 and Figure 6.19 show the detailed dimension of the SC and how the SC is connected to the beams, respectively. Note that, the symbols 'SC-A' and 'SC-B' in Table 6.8 denote the SCs whose cross sections are C 100×50×20×2.3 and C 75×45×15×2.3, respectively. The SC was fixed with 4 bolts at each end to the top and bottom of the story beams. The actual installation of the SC at the 1st story is depicted in Figure 6.20.

The clear frame that combines with 6 SCs-A at the 1st to 3rd stories (2 SCs at each floor from 1st to 3rd stories) is defined as the 'intact (or healthy) structure'. Figure 6.21 shows a photo of the intact structure. Alternatively, the frame that incorporated with smaller SCs (to simulate a slight deterioration scenario) or without SC (to simulate a considerable deterioration scenario) is treated as 'deteriorated structure'.

Table 6.8 Dimension of the SC

| | Cross section (mm) | Area (cm ²) | Mass (kg/m) | I _x (cm ⁴) |
|------|-----------------------|----------------------------|----------------|--------------------------------------|
| SC-A | 100×50×20×2.3 | 5.14 | 4.06 | 80.7 |
| SC-B | 75×45×15×2.3 | 4.14 | 3.25 | 37.1 |

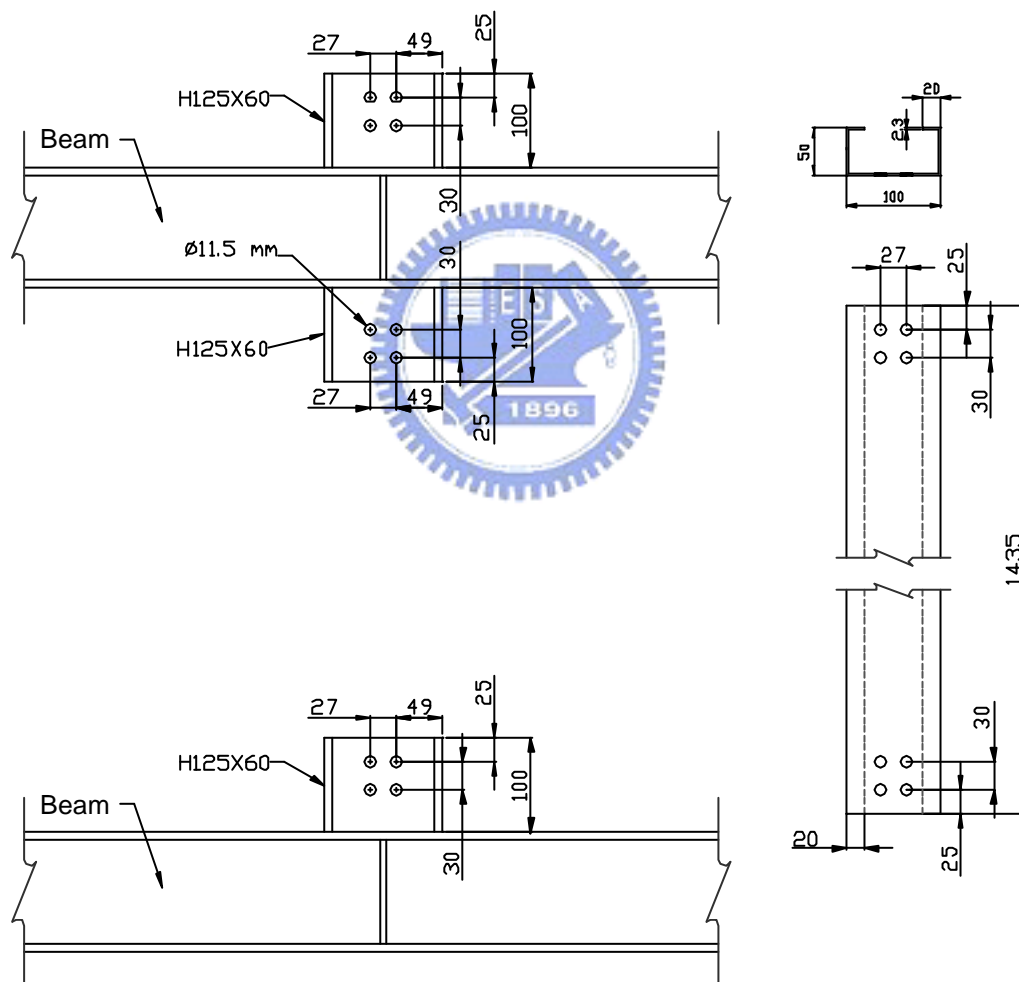


Figure 6.19 Schematic diagrams of the SC and its connection

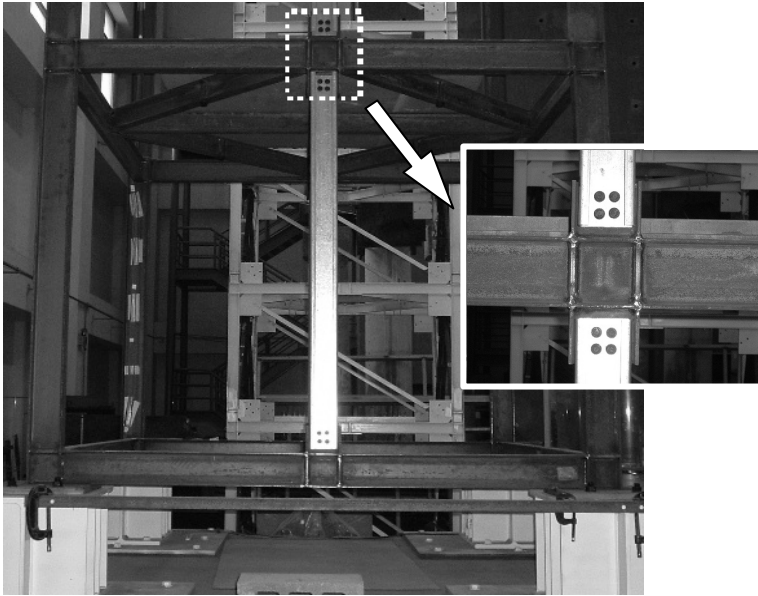


Figure 6.20 Connections of the SC at the 1st story (left) and the 2nd floor (right)



Figure 6.21 A photo of the intact structure

6.4.2 Simulated Deterioration Cases

Herein, both single-site deterioration cases and multiple-site deterioration cases are simulated. Table 6.9 lists all the deterioration cases in studying. For convenience and simplicity, certain notations to the deterioration cases are assigned. Refer to Table 6.9, the notation *AAA* represents a baseline case in which the test frame was installed with 6 SCs-A at the 1st to 3rd stories (2 SCs at each floor). The rest cases which are pre-noted with '*Dcase*' represent the deterioration cases. Furthermore, the symbols 'A', 'B', and 'N' represent SC-A, SC-B, and without SC, respectively. For example, 'A-B-N' of case *Dcase_ABN* means that the frame was installed with the SCs-A at the 1st story, the SCs-B at the 2nd story, and without SC at the 3rd story. It is seen from Table 6.9 that, *Dcase_BAA* and *Dcase_NAA* are deterioration cases in which the deterioration was induced by reduction in the story stiffness at the 1st story. Hence, the deterioration class for these cases is denoted by *Dclass_k1*. Similarly, if the SCs at the 1st and 2nd story were removed from the intact structure, this deterioration case and its corresponding deterioration class are denoted by *Dcase_NNA* and *Dclass_k1&k2*, respectively.

6.5 Experimental Scheme

Starting from the shaking table test of the intact structure, the simulated deterioration events, listed in Table 6.9, are then in turn implemented on the shaking table. The base excitation that inputs to the shaking table is the Kobe earthquake whose intensity is reduced to the level of PGA 0.08g. The sampling rate of the acceleration and RSG records is 200Hz. Table 6.10 shows the operation sequence of the shaking

table tests and how the response records are denoted for simplicity.

Table 6.9 Characterizations of the simulated deterioration cases

| No. | Notation of the deterioration case | SC arrangement (1F-2F-3F) | Notation of the deterioration class |
|-----|------------------------------------|---------------------------|---|
| 1 | AAA | A-A-A | <i>Intact</i> |
| 2 | <i>Dcase_BAA</i> | B-A-A | <i>Dclass_k₁</i> |
| 3 | <i>Dcase_NAA</i> | N-A-A | <i>Dclass_k₁</i> |
| 4 | <i>Dcase_ABA</i> | A-B-A | <i>Dclass_k₂</i> |
| 5 | <i>Dcase_ANA</i> | A-N-A | <i>Dclass_k₂</i> |
| 6 | <i>Dcase_AAB</i> | A-A-B | <i>Dclass_k₃</i> |
| 7 | <i>Dcase_AAN</i> | A-A-N | <i>Dclass_k₃</i> |
| 8 | <i>Dcase_BBA</i> | B-B-A | <i>Dclass_k₁&k₂</i> |
| 9 | <i>Dcase_BNA</i> | B-N-A | <i>Dclass_k₁&k₂</i> |
| 10 | <i>Dcase_NBA</i> | N-B-A | <i>Dclass_k₁&k₂</i> |
| 11 | <i>Dcase_NNA</i> | N-N-A | <i>Dclass_k₁&k₂</i> |
| 12 | <i>Dcase_BAB</i> | B-A-B | <i>Dclass_k₁&k₃</i> |
| 13 | <i>Dcase_BAN</i> | B-A-N | <i>Dclass_k₁&k₃</i> |
| 14 | <i>Dcase_NAB</i> | N-A-B | <i>Dclass_k₁&k₃</i> |
| 15 | <i>Dcase_NAN</i> | N-A-N | <i>Dclass_k₁&k₃</i> |
| 16 | <i>Dcase_ABB</i> | A-B-B | <i>Dclass_k₂&k₃</i> |
| 17 | <i>Dcase_ABN</i> | A-B-N | <i>Dclass_k₂&k₃</i> |
| 18 | <i>Dcase_ANB</i> | A-N-B | <i>Dclass_k₂&k₃</i> |
| 19 | <i>Dcase_ANN</i> | A-N-N | <i>Dclass_k₂&k₃</i> |
| 20 | <i>Dcase_BBB</i> | B-B-B | <i>Dclass_k₁&k₂&k₃</i> |
| 21 | <i>Dcase_BBN</i> | B-B-N | <i>Dclass_k₁&k₂&k₃</i> |
| 22 | <i>Dcase_NBB</i> | N-B-B | <i>Dclass_k₁&k₂&k₃</i> |
| 23 | <i>Dcase_BNN</i> | B-N-N | <i>Dclass_k₁&k₂&k₃</i> |
| 24 | <i>Dcase_NNB</i> | N-N-B | <i>Dclass_k₁&k₂&k₃</i> |
| 25 | <i>Dcase_NNN</i> | N-N-N | <i>Dclass_k₁&k₂&k₃</i> |

Table 6.10 Operation sequence of the shaking table tests

| Case | Save acc. data as | Save RSG data as | Save FBG data as |
|------------------|--------------------------|-------------------------|-------------------------|
| <i>AAA</i> | <i>AAA_acc</i> | <i>AAA_RSG</i> | <i>AAA_FBG</i> |
| <i>Dcase_BAA</i> | <i>BAA_acc</i> | <i>BAA_RSG</i> | <i>BAA_FBG</i> |
| <i>Dcase_NAA</i> | <i>NAA_acc</i> | <i>NAA_RSG</i> | <i>NAA_FBG</i> |
| <i>Dcase_ABA</i> | <i>ABA_acc</i> | <i>ABA_RSG</i> | <i>ABA_FBG</i> |
| <i>Dcase_ANA</i> | <i>ANA_acc</i> | <i>ANA_RSG</i> | <i>ANA_FBG</i> |
| <i>Dcase_AAB</i> | <i>AAB_acc</i> | <i>AAB_RSG</i> | <i>AAB_FBG</i> |
| <i>Dcase_AAN</i> | <i>AAN_acc</i> | <i>AAN_RSG</i> | <i>AAN_FBG</i> |
| <i>Dcase_BBA</i> | <i>BBA_acc</i> | <i>BBA_RSG</i> | <i>BBA_FBG</i> |
| <i>Dcase_BNA</i> | <i>BNA_acc</i> | <i>BNA_RSG</i> | <i>BNA_FBG</i> |
| <i>Dcase_NBA</i> | <i>NBA_acc</i> | <i>NBA_RSG</i> | <i>NBA_FBG</i> |
| <i>Dcase_NNA</i> | <i>NNA_acc</i> | <i>NNA_RSG</i> | <i>NNA_FBG</i> |
| <i>Dcase_BAB</i> | <i>BAB_acc</i> | <i>BAB_RSG</i> | <i>BAB_FBG</i> |
| <i>Dcase_BAN</i> | <i>BAN_acc</i> | <i>BAN_RSG</i> | <i>BAN_FBG</i> |
| <i>Dcase_NAB</i> | <i>NAB_acc</i> | <i>NAB_RSG</i> | <i>NAB_FBG</i> |
| <i>Dcase_NAN</i> | <i>NAN_acc</i> | <i>NAN_RSG</i> | <i>NAN_FBG</i> |
| <i>Dcase_ABB</i> | <i>ABB_acc</i> | <i>ABB_RSG</i> | <i>ABB_FBG</i> |
| <i>Dcase_ABN</i> | <i>ABN_acc</i> | <i>ABN_RSG</i> | <i>ABN_FBG</i> |
| <i>Dcase_ANB</i> | <i>ANB_acc</i> | <i>ANB_RSG</i> | <i>ANB_FBG</i> |
| <i>Dcase_ANN</i> | <i>ANN_acc</i> | <i>ANN_RSG</i> | <i>ANN_FBG</i> |
| <i>Dcase_BBB</i> | <i>BBB_acc</i> | <i>BBB_RSG</i> | <i>BBB_FBG</i> |
| <i>Dcase_BBN</i> | <i>BBN_acc</i> | <i>BBN_RSG</i> | <i>BBN_FBG</i> |
| <i>Dcase_NBB</i> | <i>NBB_acc</i> | <i>NBB_RSG</i> | <i>NBB_FBG</i> |
| <i>Dcase_BNN</i> | <i>BNN_acc</i> | <i>BNN_RSG</i> | <i>BNN_FBG</i> |
| <i>Dcase_NNB</i> | <i>NNB_acc</i> | <i>NNB_RSG</i> | <i>NNB_FBG</i> |
| <i>Dcase_NNN</i> | <i>NNN_acc</i> | <i>NNN_RSG</i> | <i>NNN_FBG</i> |

6.6 Pre-Analysis Of The Measured Data

6.6.1 Acceleration Records and their Fourier Spectra

Some statistical properties about the acceleration measurements are listed in Table 6.11. According to the statistics, several findings are discussed as follow.

- (1) Because the input excitations for each shaking table test are the same, the influence of the induced deterioration to the test frame can be directly discussed basing on the structural response.
- (2) The effect of replacing the smaller SCs (SC-B in Table 6.8), according to Table 6.11, is much lesser than that of removing the SCs. For example, the measurements of the deterioration case D_{case_BAA} are slightly higher than that of the intact case AAA (the $\Delta_{max}(acc.) = 0.001, 0.010, 0.009, 0.023$); in contrast, the measurements of D_{case_NAA} increase significantly (the $\Delta_{max}(acc.) = 0.012, 0.025, 0.039, 0.014$). Similar situations also happen to other deterioration cases, such as D_{case_ABA} and D_{case_ANA} , D_{case_AAB} and D_{case_AAN} , etc. This phenomenon is welcome because it meets the requirement for studying both the low-level and high-level deterioration in the structure. For the convenience of comparison, the increments of maximum response for low-level and high-level single-site deterioration scenarios are shown in Figure 6.22.
- (3) Due to the insignificance of replacing the SC-A with SC-B to the structure, the measurement discrepancy between each other is small (i.e. the responses are similar to each other), especially when the SCs were replaced from only one story. For instance, compare the case AAA with D_{case_AAB} whose SCs

at the 3rd story were replaced with SCs-B, the relative increments of the maximum response for each floor are only -3.9%, 6.0%, 4.9%, and 0.8%. Similar situations also happen to *Dcase_ANA* and *Dcase_BNA*, *Dcase_NAA* and *Dcase_NBA*, and *Dcase_AAN* and *Dcase_ABN* (Figure 6.23), etc.

- (4) Following with the finding 3, this phenomenon could possibly lead to similar identification results of modal parameters.

For a time series record, the most preliminary analysis approach adopted is to obtain its Fourier spectrum. From the spectrum, the distribution of the modal frequencies can be roughly identified. Figure 6.24 shows the spectra of the acceleration responses (i.e. AAA_acc) at each floor for the intact structure. According to the spectra, the first four modal frequencies of the intact structure are about 1.7, 5.0, 8.1, and 10.2Hz (peaks in the figure). The information from the Fourier spectrum is helpful for detailed modal analysis. Comparisons of the spectra for each deterioration class are also made between the intact and deteriorated structure, and they are shown in Figures 6.25 to 6.31. Note that in those figures, the observed responses at the 4th floor (4F) were used to generate the spectra. It is evidently seen (Figure 6.31, especially) from those figures that, with increasing deterioration extent the modal frequencies of the deteriorated structure shift larger from the baseline (i.e. modal frequencies of the intact structure). Consequently, it is foreseeable that, the changes in structural modal parameters of the test frame would be successfully identified through the system identification techniques such as ANNSI model.

Table 6.11 Statistical summaries of the acceleration records

| Case | I. Max. response (g) max(<i>acc.</i>) | | | | II. Standard deviation (g) std(<i>acc.</i>) | | | |
|-----------|--|-------|-------|-------|--|-------|-------|-------|
| | 1F | 2F | 3F | 4F | 1F | 2F | 3F | 4F |
| AAA | 0.095 | 0.119 | 0.131 | 0.177 | 0.016 | 0.023 | 0.028 | 0.035 |
| Dcase_BAA | 0.096 | 0.129 | 0.140 | 0.200 | 0.018 | 0.027 | 0.034 | 0.041 |
| Dcase_NAA | 0.107 | 0.144 | 0.170 | 0.191 | 0.028 | 0.038 | 0.046 | 0.057 |
| Dcase_ABA | 0.093 | 0.124 | 0.142 | 0.181 | 0.020 | 0.030 | 0.036 | 0.045 |
| Dcase_ANA | 0.095 | 0.145 | 0.160 | 0.204 | 0.021 | 0.038 | 0.047 | 0.056 |
| Dcase_AAB | 0.091 | 0.126 | 0.137 | 0.178 | 0.019 | 0.028 | 0.034 | 0.042 |
| Dcase_AAN | 0.117 | 0.149 | 0.157 | 0.180 | 0.021 | 0.030 | 0.037 | 0.045 |
| Dcase_BBA | 0.094 | 0.123 | 0.144 | 0.175 | 0.019 | 0.030 | 0.038 | 0.045 |
| Dcase_BNA | 0.093 | 0.143 | 0.167 | 0.202 | 0.021 | 0.037 | 0.048 | 0.056 |
| Dcase_NBA | 0.106 | 0.143 | 0.166 | 0.207 | 0.028 | 0.042 | 0.052 | 0.062 |
| Dcase_NNA | 0.102 | 0.156 | 0.184 | 0.244 | 0.033 | 0.058 | 0.074 | 0.085 |
| Dcase_BAB | 0.102 | 0.138 | 0.160 | 0.184 | 0.022 | 0.032 | 0.039 | 0.048 |
| Dcase_BAN | 0.137 | 0.172 | 0.159 | 0.218 | 0.028 | 0.036 | 0.04 | 0.052 |
| Dcase_NAB | 0.104 | 0.148 | 0.192 | 0.216 | 0.027 | 0.043 | 0.054 | 0.063 |
| Dcase_NAN | 0.143 | 0.189 | 0.188 | 0.235 | 0.036 | 0.048 | 0.056 | 0.070 |
| Dcase_ABB | 0.097 | 0.131 | 0.141 | 0.184 | 0.022 | 0.033 | 0.039 | 0.048 |
| Dcase_ABN | 0.115 | 0.150 | 0.152 | 0.181 | 0.023 | 0.034 | 0.043 | 0.052 |
| Dcase_ANB | 0.095 | 0.161 | 0.171 | 0.225 | 0.023 | 0.040 | 0.051 | 0.060 |
| Dcase_ANN | 0.100 | 0.158 | 0.162 | 0.230 | 0.026 | 0.043 | 0.055 | 0.066 |
| Dcase_BBB | 0.089 | 0.129 | 0.152 | 0.184 | 0.024 | 0.035 | 0.042 | 0.051 |
| Dcase_BBN | 0.130 | 0.170 | 0.160 | 0.221 | 0.030 | 0.041 | 0.046 | 0.058 |
| Dcase_NBB | 0.103 | 0.159 | 0.201 | 0.227 | 0.036 | 0.059 | 0.074 | 0.087 |
| Dcase_BNN | 0.135 | 0.171 | 0.179 | 0.265 | 0.034 | 0.053 | 0.065 | 0.078 |
| Dcase_NNB | 0.098 | 0.148 | 0.193 | 0.248 | 0.043 | 0.079 | 0.099 | 0.115 |
| Dcase_NNN | 0.133 | 0.184 | 0.210 | 0.298 | 0.050 | 0.084 | 0.109 | 0.127 |

Table 6.11 (Continue)

| Case | III. $\Delta \max(\text{acc.})$ (g) (= <i>deterioration case</i> - <i>baseline</i>) | | | | IV. $\Delta \max(\text{acc.})/\text{baseline}$ (%) | | | |
|-----------|---|-------|-------|--------|--|------|------|------|
| | 1F | 2F | 3F | 4F | 1F | 2F | 3F | 4F |
| AAA | / | / | / | / | / | / | / | / |
| Dcase_BAA | 0.001 | 0.010 | 0.009 | 0.023 | 0.6 | 8.3 | 6.9 | 13.0 |
| Dcase_NAA | 0.012 | 0.025 | 0.039 | 0.014 | 12.3 | 21.0 | 29.5 | 7.9 |
| Dcase_ABA | -0.002 | 0.005 | 0.011 | 0.004 | -1.8 | 4.3 | 8.0 | 2.0 |
| Dcase_ANA | 0.000 | 0.026 | 0.029 | 0.027 | 0.2 | 21.7 | 22.1 | 15.0 |
| Dcase_AAB | -0.004 | 0.007 | 0.006 | 0.001 | -3.9 | 6.0 | 4.9 | 0.8 |
| Dcase_AAN | 0.022 | 0.030 | 0.026 | 0.003 | 23.6 | 24.8 | 19.8 | 1.5 |
| Dcase_BBA | -0.001 | 0.004 | 0.013 | -0.002 | -1.6 | 3.0 | 10.2 | -1.4 |
| Dcase_BNA | -0.002 | 0.024 | 0.036 | 0.025 | -1.9 | 20.0 | 27.5 | 13.9 |
| Dcase_NBA | 0.011 | 0.024 | 0.035 | 0.030 | 11.2 | 20.1 | 27.0 | 16.9 |
| Dcase_NNA | 0.007 | 0.037 | 0.053 | 0.067 | 7.4 | 31.1 | 40.5 | 37.9 |
| Dcase_BAB | 0.007 | 0.019 | 0.029 | 0.007 | 7.5 | 15.9 | 22.1 | 4.1 |
| Dcase_BAN | 0.042 | 0.053 | 0.028 | 0.041 | 44.7 | 44.8 | 21.4 | 23.4 |
| Dcase_NAB | 0.009 | 0.029 | 0.061 | 0.039 | 9.2 | 24.5 | 46.9 | 22.2 |
| Dcase_NAN | 0.048 | 0.070 | 0.057 | 0.058 | 50.5 | 58.7 | 43.3 | 32.6 |
| Dcase_ABB | 0.002 | 0.012 | 0.010 | 0.007 | 2.6 | 10.3 | 7.3 | 3.7 |
| Dcase_ABN | 0.020 | 0.031 | 0.021 | 0.004 | 21.4 | 25.7 | 15.8 | 2.1 |
| Dcase_ANB | 0.000 | 0.042 | 0.040 | 0.048 | 0.4 | 35.4 | 30.5 | 26.9 |
| Dcase_ANN | 0.005 | 0.039 | 0.031 | 0.053 | 5.3 | 32.8 | 23.7 | 29.9 |
| Dcase_BBB | -0.006 | 0.010 | 0.021 | 0.007 | -6.3 | 8.4 | 16.0 | 4.0 |
| Dcase_BBN | 0.035 | 0.051 | 0.029 | 0.044 | 36.7 | 43.2 | 22.1 | 25.0 |
| Dcase_NBB | 0.008 | 0.040 | 0.070 | 0.050 | 8.0 | 33.6 | 53.5 | 28.1 |
| Dcase_BNN | 0.040 | 0.052 | 0.048 | 0.088 | 42.1 | 43.7 | 36.6 | 49.7 |
| Dcase_NNB | 0.003 | 0.029 | 0.062 | 0.071 | 2.7 | 24.6 | 47.5 | 40.0 |
| Dcase_NNN | 0.038 | 0.065 | 0.079 | 0.121 | 40.0 | 54.5 | 60.2 | 68.5 |

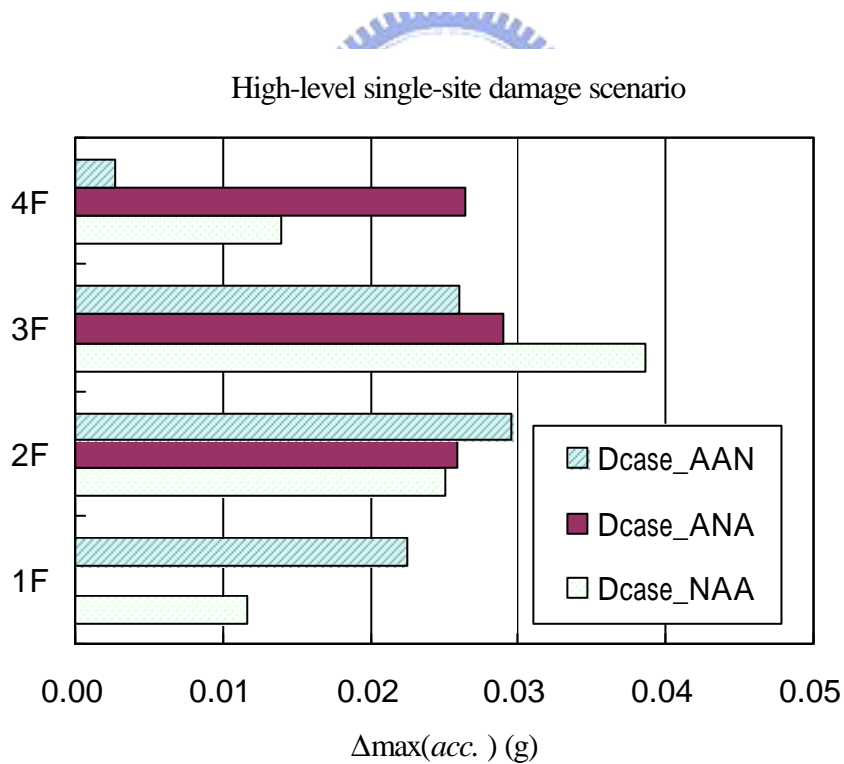
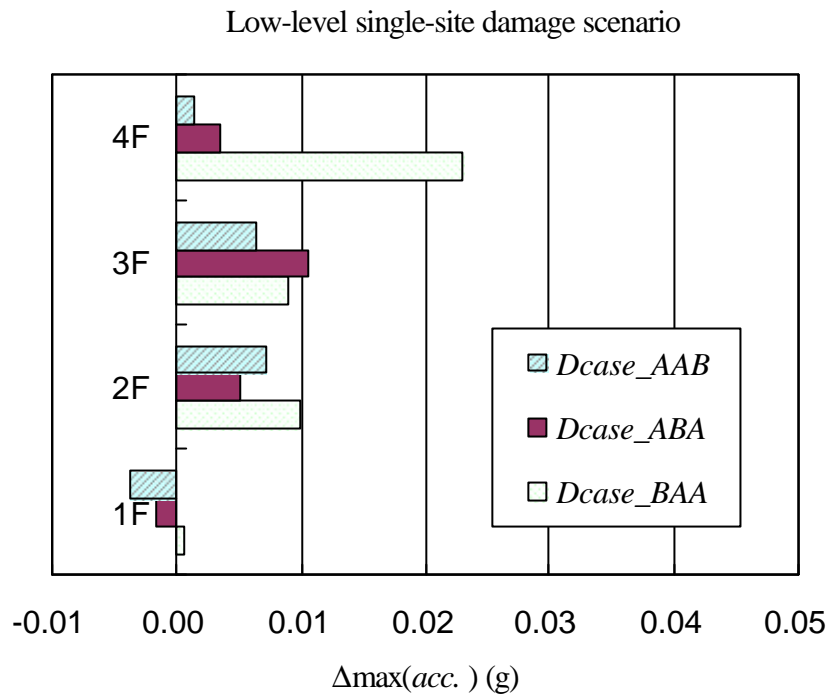


Figure 6.22 Increments of maximum response for the single-site deterioration scenarios

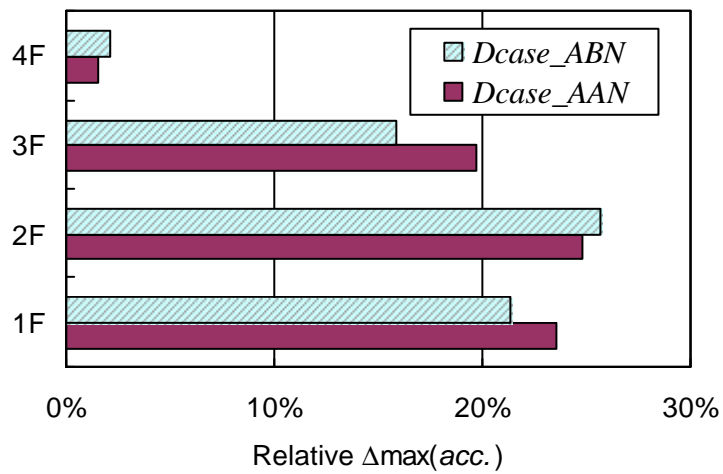
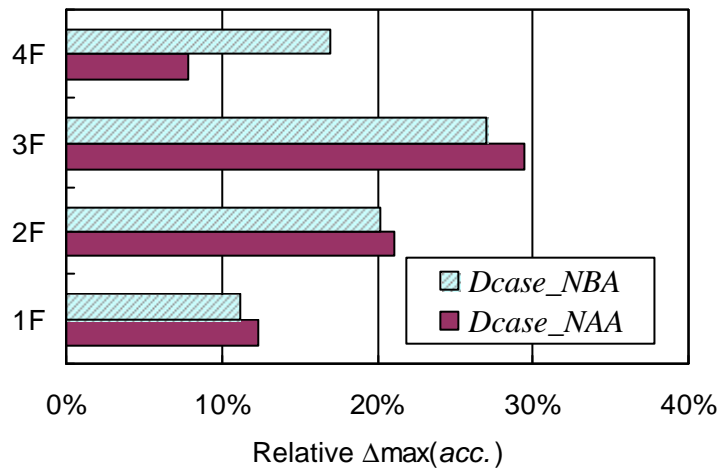
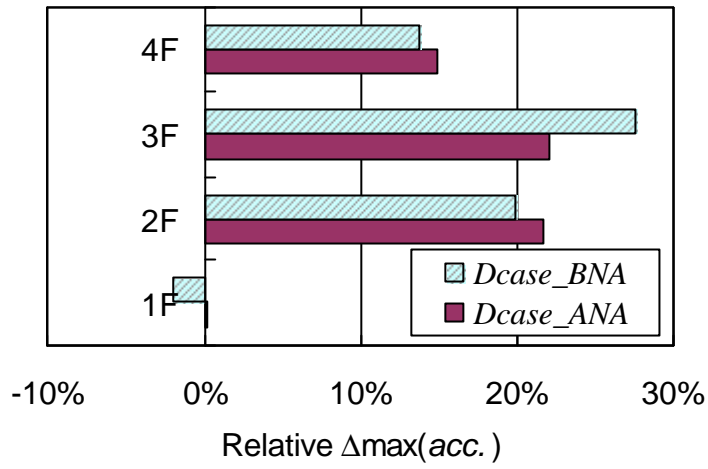


Figure 6.23 Comparisons of the effectiveness between the SC-A and SC-B

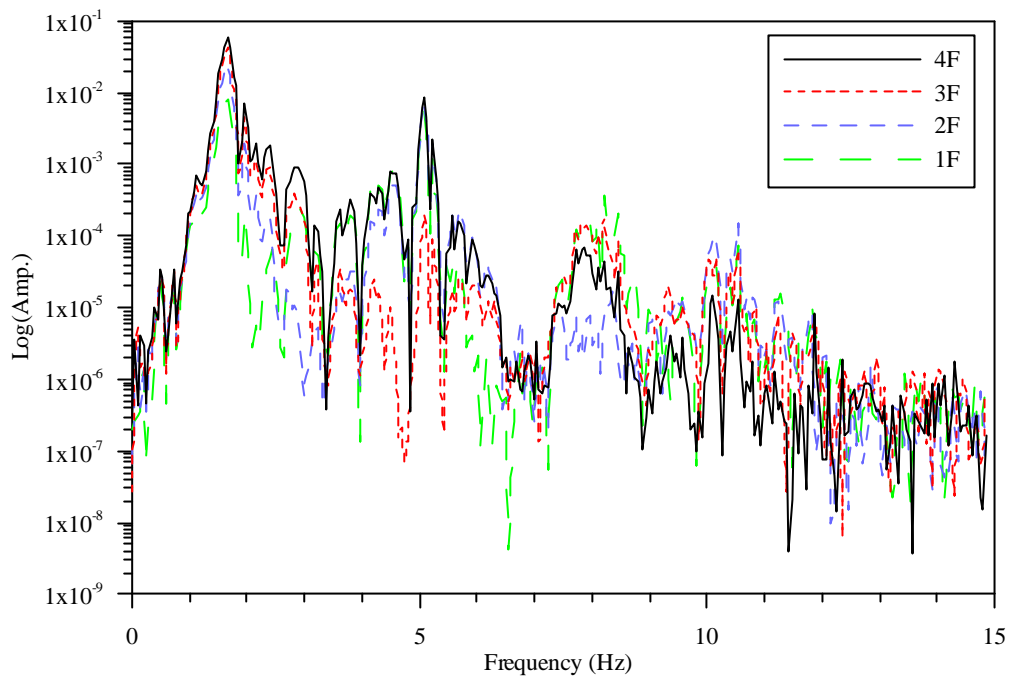


Figure 6.24 Spectra of the AAA_acc record

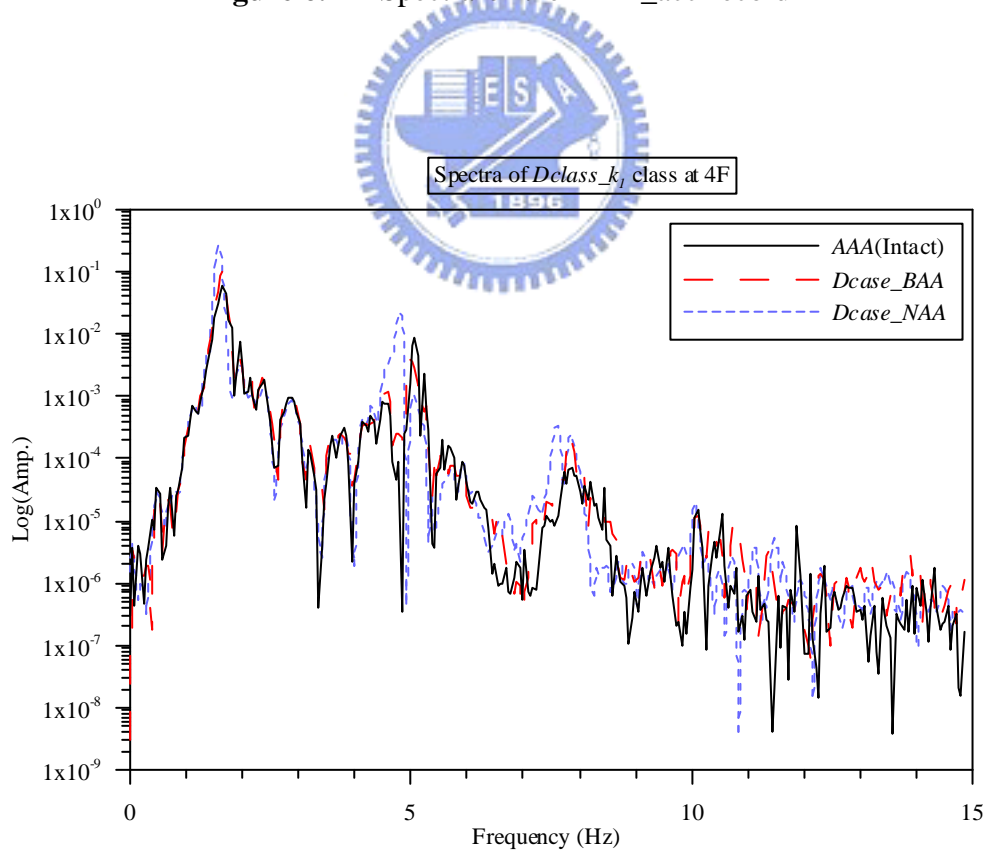


Figure 6.25 Spectra of the deterioration class $Dclass_{k_1}$

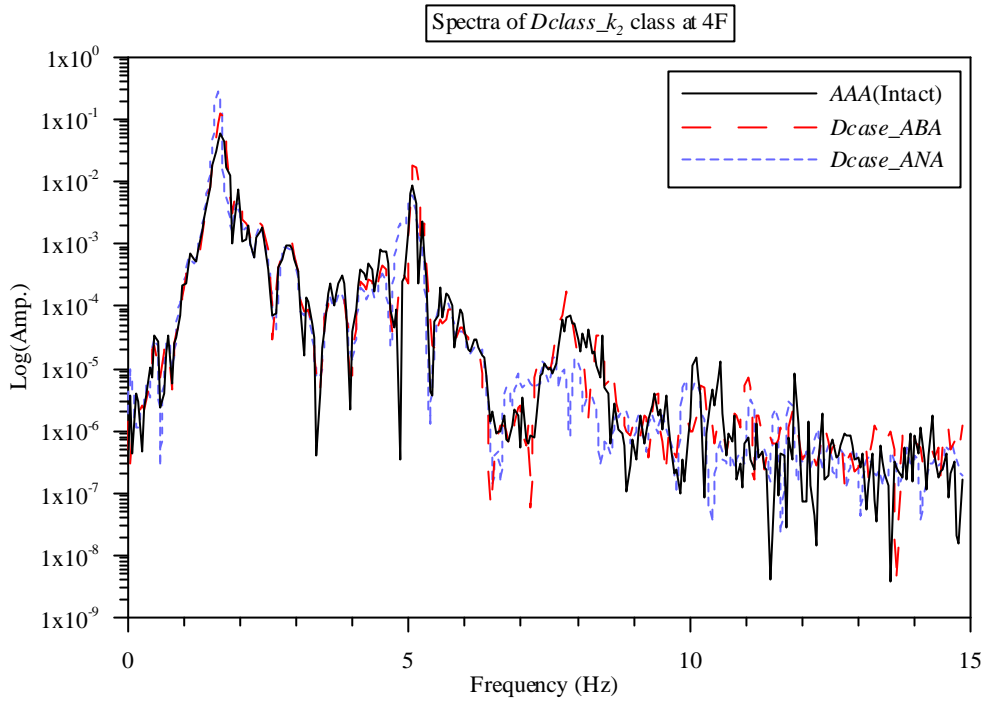


Figure 6.26 Spectra of the deterioration class $Dclass_{k_2}$

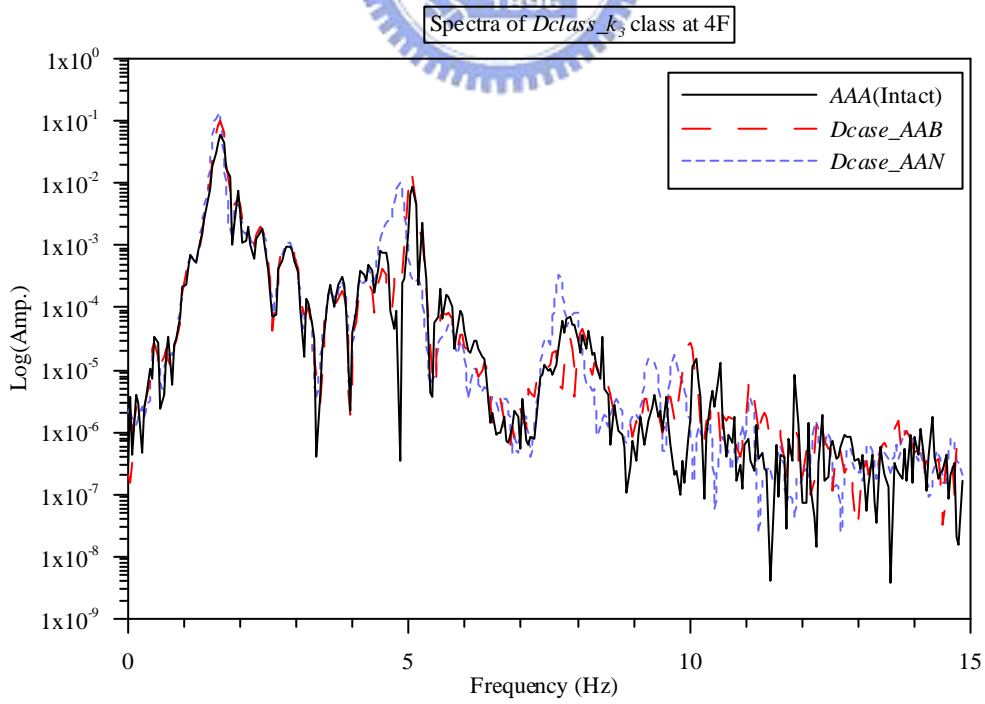


Figure 6.27 Spectra of the deterioration class $Dclass_{k_3}$

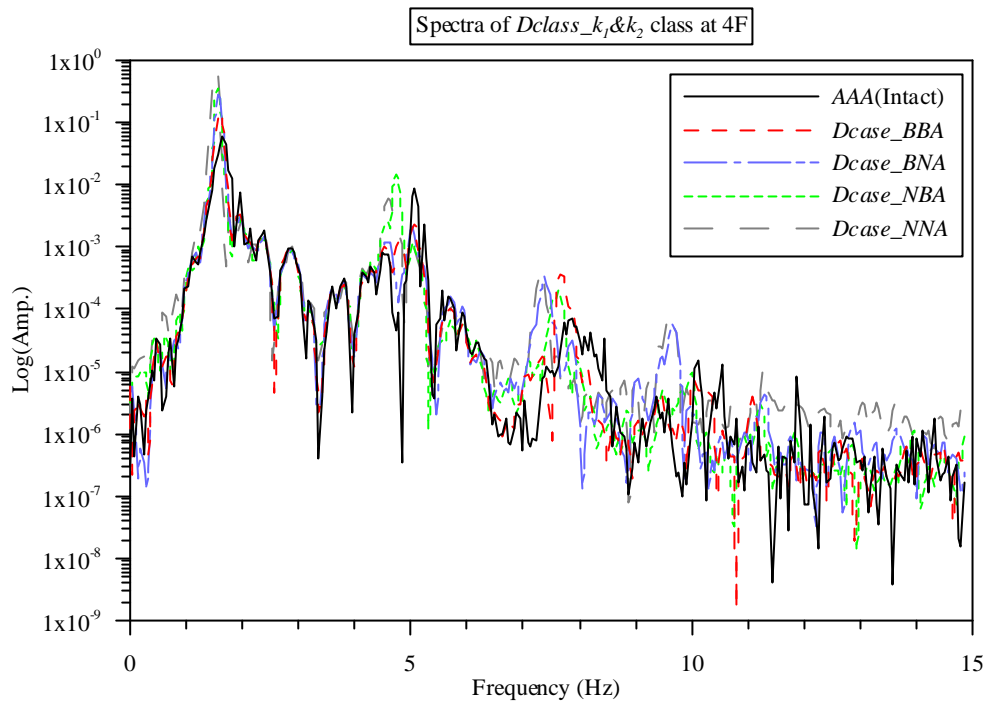


Figure 6.28 Spectra of the deterioration class $Dclass_{k_1 \& k_2}$

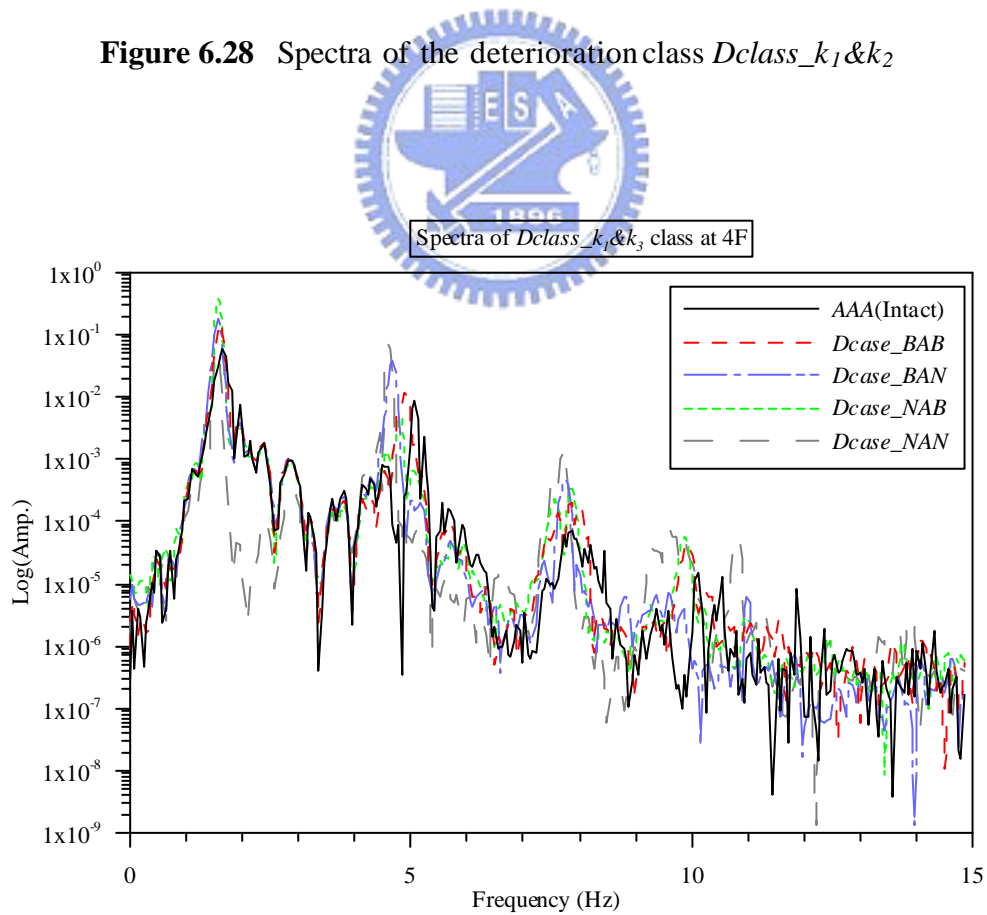


Figure 6.29 Spectra of the deterioration class $Dclass_{k_1 \& k_3}$

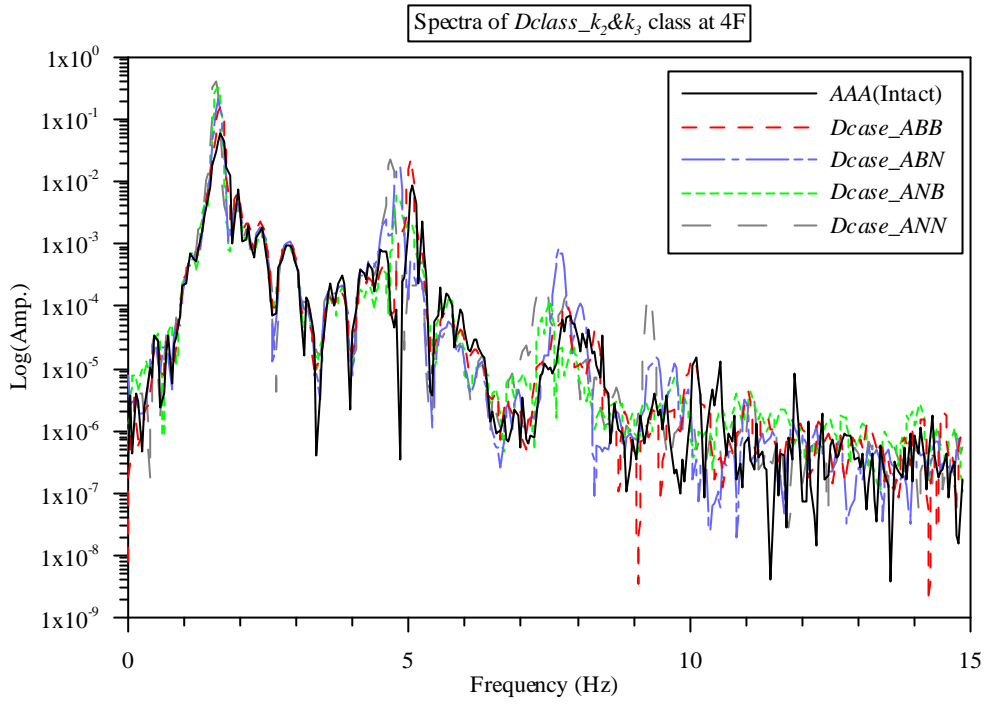


Figure 6.30 Spectra of the deterioration class $Dclass_{k_2 \& k_3}$

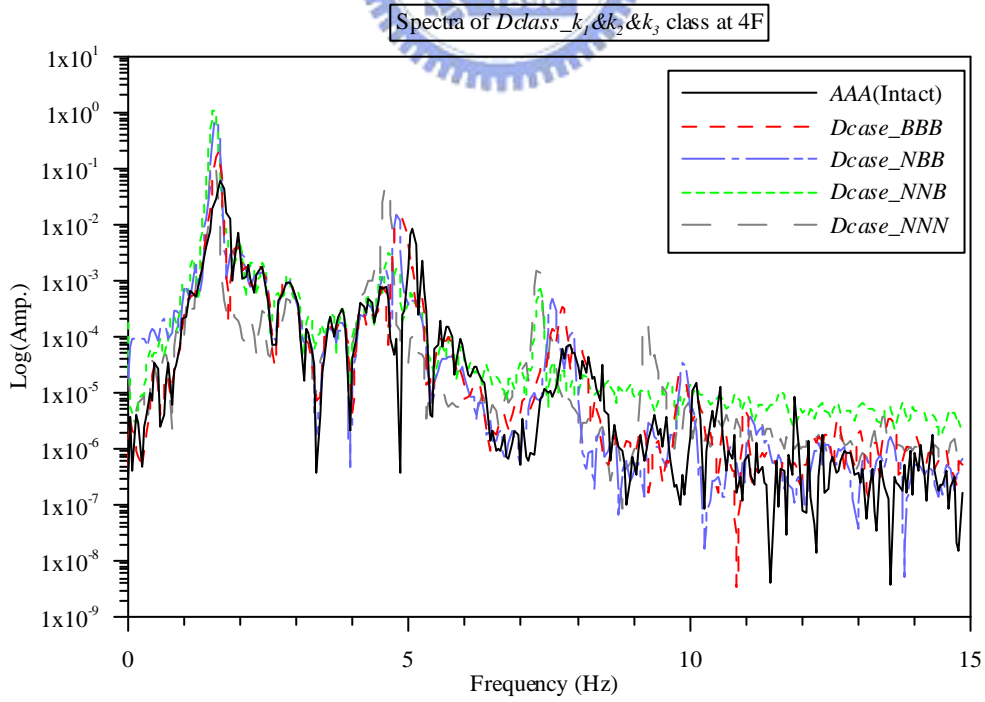


Figure 6.31 Spectra of the deterioration class $Dclass_{k_1 \& k_2 \& k_3}$

6.6.2 Measurements from the FBG Sensors and RSGs

As mentioned previously, 12 FBG sensors were configured along two fiber links, Channel 1 and Channel 2. These 12 FBG sensors are further classified, according to their locations, into three groups: the sensors which located near the bottom of the story columns on east side (i.e. FBG1, FBG3, FBG5, and FBG7) will be shortly called ‘sensors at BE’; the sensors which located near the top of the story columns on east side (i.e. FBG2, FBG4, FBG6, and FBG8) will be shortly called ‘sensors at TE’; and the sensors which located near the bottom of the story columns on west side (i.e. FBG9 to FBG12) will be shortly called ‘sensors at BW’. Statistical results of the FBG sensors’ records, based on the three groups, are summarized in Tables 6.12 to 6.14, respectively. Meanwhile, statistical summaries of the RSGs’ records are shown in Table 6.15. Based on the summarized tables of the acceleration and strain measurements (Tables 6.11 to 6.15), certain findings are presented below.

- (1) Compare with the acceleration responses, the strain row data (from either FBG sensors or RSGs) shows more sensitivity to the system changes. The changes in maximum measurement of the acceleration responses (column IV, Table 6.11) are smaller than that of the strain responses (column IV, Tables 6.12 to 6.15). Take the case *Dcase_NNN* for example, the maximum relative increments in acceleration and strain responses are 68.5% (4F) and 122.3% (FBG5), respectively.
- (2) One of the major advantages of the FBG sensors is that they have better immunity to EM interference. Therefore, the signals of the FBG sensors is lesser noise-corrupted. This situation can be validated from two aspects. Firstly, according to the comparison between the FBG sensors’ and RSGs’

records (Figures 6.32 and 6.33, case AAA for example), a number of disturbances containing in the RSGs records. Secondly, the ratio, $(\frac{\text{std}(\mathbf{e})}{\max(\mathbf{e})})$, between the standard deviation of the response ($\text{std}(\mathbf{e})$) and the maximum response ($\max(\mathbf{e})$) for the RSGs' records (Table 6.15) is larger than that for the FBG sensors' records (Table 6.12).

- (3) As mentioned before, one of the functions of the RSGs is to be a reference to the FBG sensors. Thought the amplitudes of the responses of the RSGs (Figure 6.33) are lower than of the FBG sensors (Figure 6.32), the trends of these two measurements are the same.
 - (4) The FBG sensors at BE were placed at the opposite position of the story columns to the FBG sensors at TE. Therefore, the measurements they obtained should be with similar magnitude but negative phase. Take the case AAA once again for example, the correlation coefficients between the measurements of the FBG sensors at BE (Figure 6.32) and the measurements of the FBG sensors at TE (Figure 6.34) are $\{-0.9993, -0.9998, -0.9998, -0.9995\}$ which mean that these two sets of data are highly correlated in negative phase.
 - (5) Four FBG sensors (from FBG9 to FBG12) were placed at BW to have parallel location with the FBG sensors at BE so as to check torsional effect of the specimen. The discrepancy between Figures 6.32 and 6.35 is quite small, so the torsion effect is insignificant in the experiments. The correlation coefficients between the data of these two figures are $\{0.9997, 0.9989, 0.9995, 0.9985\}$ which mean that these two sets of data are highly correlated.
-

Table 6.12 Statistical summaries of the strain records from the FBG sensors at BE

| Case | I. Max. response (m strain) max(e) | | | | II. Standard deviation (m strain) std(e) | | | |
|-----------|--|-------|-------|-------|--|-------|-------|------|
| | FBG1 | FBG3 | FBG5 | FBG7 | FBG1 | FBG3 | FBG5 | FBG7 |
| AAA | 238.1 | 184.2 | 143.1 | 109.6 | 44.5 | 36.8 | 28.2 | 20.5 |
| Dcase_BAA | 256.4 | 197.7 | 155.2 | 121.2 | 56.9 | 47.1 | 35.7 | 25.1 |
| Dcase_NAA | 337.4 | 245.2 | 173.4 | 121.5 | 92.0 | 64.4 | 50.2 | 34.2 |
| Dcase_ABA | 272.0 | 215.7 | 135.6 | 117.2 | 62.8 | 53.3 | 33.2 | 27.6 |
| Dcase_ANA | 296.9 | 296.7 | 154.3 | 134.8 | 83.9 | 89.4 | 44.6 | 36.0 |
| Dcase_AAB | 264.7 | 212.4 | 144.2 | 114.4 | 52.8 | 45.3 | 31.6 | 23.5 |
| Dcase_AAN | 285.5 | 209.7 | 196.3 | 114.6 | 65.5 | 55.9 | 52.5 | 28.5 |
| Dcase_BBA | 293.0 | 219.3 | 155.0 | 113.0 | 69.7 | 55.3 | 38.8 | 26.7 |
| Dcase_BNA | 296.0 | 296.6 | 175.8 | 136.2 | 81.5 | 86.5 | 49.8 | 34.6 |
| Dcase_NBA | 349.3 | 275.7 | 192.6 | 131.9 | 105.9 | 79.9 | 56.4 | 38.1 |
| Dcase_NNA | 376.5 | 350.5 | 222.4 | 164.3 | 132.4 | 118.2 | 69.1 | 46.2 |
| Dcase_BAB | 302.1 | 230.9 | 152.0 | 117.1 | 75.2 | 59.1 | 40.5 | 29.7 |
| Dcase_BAN | 332.0 | 242.9 | 233.0 | 140.4 | 75.9 | 59.8 | 55.7 | 30.9 |
| Dcase_NAB | 370.2 | 283.6 | 182.7 | 134.5 | 112.4 | 83.5 | 56.0 | 39.3 |
| Dcase_NAN | 392.9 | 281.5 | 242.5 | 143.5 | 112.6 | 83.0 | 77.0 | 41.3 |
| Dcase_ABB | 274.6 | 212.6 | 148.4 | 118.1 | 65.7 | 55.8 | 39.0 | 28.9 |
| Dcase_ABN | 298.3 | 227.0 | 200.3 | 114.4 | 72.8 | 62.1 | 59.0 | 32.2 |
| Dcase_ANB | 312.3 | 306.0 | 177.9 | 138.0 | 87.4 | 93.0 | 52.1 | 37.5 |
| Dcase_ANN | 315.0 | 315.0 | 262.2 | 150.6 | 94.6 | 100.4 | 76.7 | 40.5 |
| Dcase_BBB | 313.2 | 246.1 | 163.0 | 121.5 | 78.8 | 62.5 | 42.8 | 30.5 |
| Dcase_BBN | 350.8 | 255.7 | 243.7 | 140.1 | 86.3 | 67.9 | 62.2 | 34.5 |
| Dcase_NBB | 421.1 | 304.2 | 212.4 | 152.2 | 152.5 | 108.6 | 77.4 | 54.1 |
| Dcase_BNN | 353.8 | 335.5 | 293.1 | 174.4 | 113.0 | 107.6 | 81.4 | 43.3 |
| Dcase_NNB | 419.7 | 385.1 | 230.2 | 171.5 | 220.5 | 196.9 | 107.1 | 75.4 |
| Dcase_NNN | 427.8 | 385.8 | 318.0 | 187.0 | 195.7 | 176.9 | 129.8 | 66.9 |

Table 6.12 (Continue)

| Case | III. $\frac{\text{std}(\mathbf{e})}{\text{max}(\mathbf{e})}$ (%) | | | | IV. $\Delta \text{max}(\mathbf{e}) / \text{baseline}$ (%) | | | |
|-----------|--|------|------|------|---|-------|-------|------|
| | FBG1 | FBG3 | FBG5 | FBG7 | FBG1 | FBG3 | FBG5 | FBG7 |
| AAA | 18.7 | 20.0 | 19.7 | 18.7 | / | / | / | / |
| Dcase_BAA | 22.2 | 23.8 | 23.0 | 20.7 | 7.7 | 7.4 | 8.5 | 10.6 |
| Dcase_NAA | 27.3 | 26.3 | 28.9 | 28.1 | 41.7 | 33.1 | 21.2 | 10.9 |
| Dcase_ABA | 23.1 | 24.7 | 24.5 | 23.6 | 14.2 | 17.1 | -5.2 | 6.9 |
| Dcase_ANA | 28.3 | 30.1 | 28.9 | 26.7 | 24.7 | 61.1 | 7.9 | 23.0 |
| Dcase_AAB | 19.9 | 21.3 | 21.9 | 20.5 | 11.2 | 15.3 | 0.8 | 4.4 |
| Dcase_AAN | 23.0 | 26.7 | 26.8 | 24.8 | 19.9 | 13.8 | 37.2 | 4.6 |
| Dcase_BBA | 23.8 | 25.2 | 25.0 | 23.7 | 23.1 | 19.1 | 8.4 | 3.1 |
| Dcase_BNA | 27.5 | 29.2 | 28.3 | 25.4 | 24.3 | 61.1 | 22.9 | 24.3 |
| Dcase_NBA | 30.3 | 29.0 | 29.3 | 28.9 | 46.7 | 49.7 | 34.6 | 20.4 |
| Dcase_NNA | 35.2 | 33.7 | 31.1 | 28.1 | 58.1 | 90.3 | 55.4 | 49.9 |
| Dcase_BAB | 24.9 | 25.6 | 26.6 | 25.4 | 26.9 | 25.4 | 6.3 | 6.9 |
| Dcase_BAN | 22.9 | 24.6 | 23.9 | 22.0 | 39.4 | 31.9 | 62.9 | 28.1 |
| Dcase_NAB | 30.4 | 29.4 | 30.6 | 29.3 | 55.5 | 54.0 | 27.7 | 22.7 |
| Dcase_NAN | 28.7 | 29.5 | 31.8 | 28.8 | 65.0 | 52.9 | 69.5 | 30.9 |
| Dcase_ABB | 23.9 | 26.3 | 26.3 | 24.5 | 15.3 | 15.4 | 3.7 | 7.7 |
| Dcase_ABN | 24.4 | 27.3 | 29.4 | 28.1 | 25.3 | 23.2 | 40.0 | 4.4 |
| Dcase_ANB | 28.0 | 30.4 | 29.3 | 27.2 | 31.2 | 66.1 | 24.4 | 25.9 |
| Dcase_ANN | 30.0 | 31.9 | 29.2 | 26.9 | 32.3 | 71.0 | 83.3 | 37.4 |
| Dcase_BBB | 25.2 | 25.4 | 26.3 | 25.1 | 31.5 | 33.6 | 14.0 | 10.9 |
| Dcase_BBN | 24.6 | 26.5 | 25.5 | 24.6 | 47.4 | 38.8 | 70.3 | 27.8 |
| Dcase_NBB | 36.2 | 35.7 | 36.4 | 35.5 | 76.9 | 65.2 | 48.4 | 38.9 |
| Dcase_BNN | 31.9 | 32.1 | 27.8 | 24.8 | 48.6 | 82.2 | 104.8 | 59.1 |
| Dcase_NNB | 52.5 | 51.1 | 46.5 | 44.0 | 76.3 | 109.1 | 60.9 | 56.5 |
| Dcase_NNN | 45.7 | 45.9 | 40.8 | 35.8 | 79.7 | 109.5 | 122.3 | 70.6 |

Table 6.13 Statistical summaries of the strain records from FBG the sensors at TE

| Case | I. Max. response (m strain) max(e) | | | | II. Standard deviation (m strain) std(e) | | | |
|-----------|--|-------|-------|-------|--|-------|-------|------|
| | FBG2 | FBG4 | FBG6 | FBG8 | FBG2 | FBG4 | FBG6 | FBG8 |
| AAA | 241.5 | 188.2 | 151.5 | 111.6 | 46.1 | 37.8 | 30.1 | 20.9 |
| Dcase_BAA | 266.8 | 202.7 | 163.5 | 122.5 | 60.1 | 48.3 | 38.1 | 25.5 |
| Dcase_NAA | 350.3 | 251.7 | 186.6 | 124.2 | 95.9 | 66.8 | 53.5 | 34.7 |
| Dcase_ABA | 277.1 | 219.3 | 146.0 | 119.2 | 64.8 | 54.3 | 35.9 | 28.2 |
| Dcase_ANA | 299.0 | 300.2 | 169.0 | 136.1 | 85.2 | 90.7 | 49.4 | 36.4 |
| Dcase_AAB | 269.4 | 216.7 | 154.7 | 117.6 | 54.6 | 46.1 | 34.2 | 24.0 |
| Dcase_AAN | 287.3 | 210.9 | 208.8 | 119.6 | 67.7 | 56.3 | 55.6 | 29.9 |
| Dcase_BBA | 298.9 | 224.3 | 166.3 | 115.1 | 71.5 | 56.4 | 41.8 | 27.3 |
| Dcase_BNA | 300.8 | 294.6 | 193.6 | 138.5 | 83.7 | 86.2 | 54.7 | 35.2 |
| Dcase_NBA | 358.1 | 280.3 | 209.4 | 133.3 | 109.2 | 81.7 | 60.8 | 38.7 |
| Dcase_NNA | 384.2 | 350.1 | 243.3 | 167.2 | 135.5 | 118.2 | 75.8 | 47.2 |
| Dcase_BAB | 307.5 | 236.6 | 163.4 | 118.8 | 77.4 | 60.9 | 43.6 | 30.3 |
| Dcase_BAN | 331.2 | 245.0 | 245.6 | 147.1 | 77.9 | 60.8 | 58.7 | 32.5 |
| Dcase_NAB | 379.7 | 291.9 | 196.4 | 137.0 | 116.6 | 86.3 | 60.4 | 39.9 |
| Dcase_NAN | 397.6 | 286.1 | 254.7 | 150.5 | 116.5 | 84.8 | 80.7 | 43.5 |
| Dcase_ABB | 277.9 | 215.9 | 159.2 | 120.6 | 67.7 | 56.7 | 42.0 | 29.7 |
| Dcase_ABN | 302.6 | 226.7 | 211.3 | 118.9 | 75.3 | 62.3 | 62.6 | 33.8 |
| Dcase_ANB | 314.0 | 307.7 | 195.5 | 140.1 | 88.8 | 94.0 | 57.3 | 38.1 |
| Dcase_ANN | 315.8 | 317.0 | 279.4 | 159.1 | 96.2 | 100.7 | 81.7 | 42.7 |
| Dcase_BBB | 319.8 | 249.5 | 174.6 | 126.0 | 81.0 | 63.9 | 45.9 | 31.3 |
| Dcase_BBN | 353.6 | 258.2 | 257.5 | 147.0 | 88.7 | 68.7 | 65.7 | 36.2 |
| Dcase_NBB | 427.0 | 314.4 | 229.6 | 153.4 | 155.8 | 113.2 | 83.5 | 54.5 |
| Dcase_BNN | 354.9 | 336.9 | 312.2 | 183.1 | 114.8 | 108.0 | 86.9 | 45.7 |
| Dcase_NNB | 429.7 | 387.2 | 251.8 | 174.6 | 226.1 | 198.1 | 118.1 | 76.8 |
| Dcase_NNN | 434.72 | 384.2 | 338.5 | 196.8 | 201.2 | 176.7 | 138.7 | 70.8 |

Table 6.13 (Continue)

| Case | III. $\frac{\text{std}(\mathbf{e})}{\text{max}(\mathbf{e})}$ (%) | | | | IV. $\Delta \text{max}(\mathbf{e}) / \text{baseline}$ (%) | | | |
|-----------|--|------|------|------|---|-------|-------|------|
| | FBG2 | FBG4 | FBG6 | FBG8 | FBG2 | FBG4 | FBG6 | FBG8 |
| AAA | 19.1 | 20.1 | 19.8 | 18.7 | / | / | / | / |
| Dcase_BAA | 22.5 | 23.8 | 23.3 | 20.8 | 10.5 | 7.7 | 7.9 | 9.8 |
| Dcase_NAA | 27.4 | 26.6 | 28.7 | 28.0 | 45.0 | 33.7 | 23.2 | 11.3 |
| Dcase_ABA | 23.4 | 24.8 | 24.6 | 23.6 | 14.7 | 16.5 | -3.6 | 6.9 |
| Dcase_ANA | 28.5 | 30.2 | 29.3 | 26.7 | 23.8 | 59.5 | 11.5 | 22.0 |
| Dcase_AAB | 20.3 | 21.3 | 22.1 | 20.4 | 11.5 | 15.1 | 2.1 | 5.5 |
| Dcase_AAN | 23.6 | 26.7 | 26.6 | 25.0 | 18.9 | 12.0 | 37.8 | 7.2 |
| Dcase_BBA | 23.9 | 25.1 | 25.2 | 23.7 | 23.8 | 19.2 | 9.8 | 3.2 |
| Dcase_BNA | 27.8 | 29.3 | 28.2 | 25.4 | 24.6 | 56.5 | 27.8 | 24.2 |
| Dcase_NBA | 30.5 | 29.1 | 29.0 | 29.0 | 48.3 | 48.9 | 38.2 | 19.5 |
| Dcase_NNA | 35.3 | 33.8 | 31.2 | 28.2 | 59.1 | 86.0 | 60.6 | 49.9 |
| Dcase_BAB | 25.2 | 25.7 | 26.7 | 25.5 | 27.3 | 25.7 | 7.9 | 6.5 |
| Dcase_BAN | 23.5 | 24.8 | 23.9 | 22.1 | 37.1 | 30.2 | 62.1 | 31.9 |
| Dcase_NAB | 30.7 | 29.6 | 30.8 | 29.1 | 57.2 | 55.1 | 29.6 | 22.8 |
| Dcase_NAN | 29.3 | 29.6 | 31.7 | 28.9 | 64.6 | 52.0 | 68.1 | 34.9 |
| Dcase_ABB | 24.4 | 26.3 | 26.3 | 24.6 | 15.0 | 14.7 | 5.1 | 8.1 |
| Dcase_ABN | 24.9 | 27.5 | 29.6 | 28.4 | 25.3 | 20.4 | 39.5 | 6.6 |
| Dcase_ANB | 28.3 | 30.5 | 29.3 | 27.2 | 30.0 | 63.4 | 29.0 | 25.6 |
| Dcase_ANN | 30.5 | 31.8 | 29.2 | 26.8 | 30.7 | 68.4 | 84.4 | 42.6 |
| Dcase_BBB | 25.3 | 25.6 | 26.3 | 24.9 | 32.4 | 32.6 | 15.3 | 13.0 |
| Dcase_BBN | 25.1 | 26.6 | 25.5 | 24.6 | 46.4 | 37.2 | 70.0 | 31.8 |
| Dcase_NBB | 36.5 | 36.0 | 36.4 | 35.5 | 76.8 | 67.0 | 51.5 | 37.5 |
| Dcase_BNN | 32.3 | 32.0 | 27.8 | 24.9 | 46.9 | 79.0 | 106.1 | 64.2 |
| Dcase_NNB | 52.6 | 51.2 | 46.9 | 44.0 | 77.9 | 105.7 | 66.2 | 56.5 |
| Dcase_NNN | 46.3 | 46.0 | 41.0 | 36.0 | 80.0 | 104.1 | 123.4 | 76.4 |

Table 6.14 Statistical summaries of the strain records from the FBG sensors at BW

| Case | I. Max. response (m strain) max(e) | | | | II. Standard deviation (m strain) std(e) | | | |
|-----------|--|-------|-------|-------|--|-------|-------|-------|
| | FBG9 | FBG10 | FBG11 | FBG12 | FBG9 | FBG10 | FBG11 | FBG12 |
| AAA | 250.0 | 190.1 | 142.8 | 98.1 | 47.0 | 38.2 | 28.5 | 19.2 |
| Dcase_BAA | 275.6 | 205.4 | 155.8 | 108.1 | 61.2 | 48.8 | 36.1 | 23.4 |
| Dcase_NAA | 362.6 | 256.5 | 179.5 | 111.2 | 99.5 | 65.9 | 50.3 | 31.5 |
| Dcase_ABA | 285.4 | 221.7 | 136.5 | 109.7 | 66.1 | 54.9 | 33.9 | 26.4 |
| Dcase_ANA | 314.2 | 306.3 | 154.4 | 127.0 | 89.0 | 92.2 | 44.7 | 33.8 |
| Dcase_AAB | 278.2 | 219.8 | 144.6 | 106.9 | 55.8 | 46.8 | 32.0 | 22.4 |
| Dcase_AAN | 299.1 | 217.2 | 195.7 | 112.5 | 69.4 | 58.0 | 52.7 | 26.2 |
| Dcase_BBA | 310.6 | 227.3 | 159.4 | 108.4 | 73.8 | 57.1 | 40.4 | 25.0 |
| Dcase_BNA | 315.1 | 307.3 | 178.6 | 129.0 | 86.9 | 89.4 | 50.5 | 31.4 |
| Dcase_NBA | 371.6 | 277.5 | 198.5 | 126.1 | 113.2 | 80.7 | 57.6 | 34.9 |
| Dcase_NNA | 402.2 | 355.0 | 225.7 | 156.1 | 141.3 | 119.7 | 70.5 | 41.8 |
| Dcase_BAB | 322.4 | 239.6 | 154.4 | 114.3 | 80.4 | 61.4 | 41.1 | 28.3 |
| Dcase_BAN | 352.2 | 252.2 | 236.4 | 138.4 | 81.1 | 62.4 | 56.2 | 28.6 |
| Dcase_NAB | 398.3 | 287.4 | 181.6 | 130.8 | 121.1 | 84.8 | 56.0 | 37.0 |
| Dcase_NAN | 418.1 | 286.3 | 240.8 | 141.3 | 120.9 | 84.4 | 76.4 | 38.4 |
| Dcase_ABB | 287.4 | 220.2 | 149.7 | 108.7 | 69.2 | 57.7 | 39.6 | 26.7 |
| Dcase_ABN | 313.6 | 236.7 | 201.9 | 104.9 | 77.0 | 64.4 | 59.2 | 29.6 |
| Dcase_ANB | 330.6 | 315.5 | 179.3 | 129.3 | 92.8 | 96.0 | 52.1 | 33.9 |
| Dcase_ANN | 332.7 | 325.6 | 260.5 | 150.1 | 100.7 | 103.7 | 76.1 | 37.4 |
| Dcase_BBB | 332.2 | 254.0 | 169.2 | 124.2 | 83.6 | 64.2 | 44.4 | 29.8 |
| Dcase_BBN | 371.2 | 264.9 | 248.0 | 138.8 | 91.9 | 70.5 | 63.7 | 31.9 |
| Dcase_NBB | 449.3 | 313.1 | 212.3 | 143.4 | 163.1 | 112.3 | 76.8 | 49.3 |
| Dcase_BNN | 375.5 | 348.2 | 290.1 | 172.1 | 121.2 | 111.7 | 80.8 | 40.2 |
| Dcase_NNB | 449.3 | 389.6 | 233.2 | 167.7 | 235.9 | 199.2 | 108.1 | 70.6 |
| Dcase_NNN | 455.1 | 390.6 | 316.5 | 185.3 | 209.9 | 179.1 | 129.5 | 62.7 |

Table 6.14 (Continue)

| Case | III. $\frac{\text{std}(\mathbf{e})}{\text{max}(\mathbf{e})}$ (%) | | | | IV. $\Delta \text{max}(\mathbf{e}) / \text{baseline}$ (%) | | | |
|-----------|--|-------|-------|-------|---|-------|-------|-------|
| | FBG9 | FBG10 | FBG11 | FBG12 | FBG9 | FBG10 | FBG11 | FBG12 |
| AAA | 18.8 | 20.1 | 20.0 | 19.5 | / | / | / | / |
| Dcase_BAA | 22.2 | 23.7 | 23.2 | 21.7 | 10.2 | 8.0 | 9.1 | 10.2 |
| Dcase_NAA | 27.5 | 25.7 | 28.0 | 28.3 | 45.0 | 34.9 | 25.7 | 13.3 |
| Dcase_ABA | 23.1 | 24.8 | 24.8 | 24.1 | 14.2 | 16.6 | -4.4 | 11.8 |
| Dcase_ANA | 28.3 | 30.1 | 28.9 | 26.6 | 25.7 | 61.1 | 8.1 | 29.4 |
| Dcase_AAB | 20.1 | 21.3 | 22.1 | 21.0 | 11.3 | 15.6 | 1.3 | 8.9 |
| Dcase_AAN | 23.2 | 26.7 | 26.9 | 23.3 | 19.7 | 14.2 | 37.1 | 14.6 |
| Dcase_BBA | 23.8 | 25.1 | 25.3 | 23.0 | 24.3 | 19.6 | 11.6 | 10.4 |
| Dcase_BNA | 27.6 | 29.1 | 28.3 | 24.3 | 26.0 | 61.6 | 25.1 | 31.4 |
| Dcase_NBA | 30.5 | 29.1 | 29.0 | 27.7 | 48.7 | 46.0 | 39.0 | 28.4 |
| Dcase_NNA | 35.1 | 33.7 | 31.2 | 26.8 | 60.9 | 86.7 | 58.0 | 59.0 |
| Dcase_BAB | 24.9 | 25.6 | 26.6 | 24.8 | 29.0 | 26.0 | 8.1 | 16.4 |
| Dcase_BAN | 23.0 | 24.7 | 23.8 | 20.7 | 40.9 | 32.7 | 65.5 | 41.0 |
| Dcase_NAB | 30.4 | 29.5 | 30.8 | 28.3 | 59.3 | 51.2 | 27.2 | 33.3 |
| Dcase_NAN | 28.9 | 29.5 | 31.7 | 27.2 | 67.2 | 50.6 | 68.6 | 44.0 |
| Dcase_ABB | 24.1 | 26.2 | 26.5 | 24.6 | 15.0 | 15.8 | 4.8 | 10.8 |
| Dcase_ABN | 24.5 | 27.2 | 29.3 | 28.2 | 25.5 | 24.5 | 41.4 | 6.9 |
| Dcase_ANB | 28.1 | 30.4 | 29.1 | 26.2 | 32.2 | 66.0 | 25.6 | 31.8 |
| Dcase_ANN | 30.2 | 31.8 | 29.2 | 24.9 | 33.1 | 71.3 | 82.4 | 52.9 |
| Dcase_BBB | 25.2 | 25.3 | 26.2 | 24.0 | 32.9 | 33.6 | 18.5 | 26.5 |
| Dcase_BBN | 24.7 | 26.6 | 25.7 | 23.0 | 48.5 | 39.4 | 73.7 | 41.4 |
| Dcase_NBB | 36.3 | 35.9 | 36.2 | 34.4 | 79.7 | 64.7 | 48.7 | 46.1 |
| Dcase_BNN | 32.3 | 32.1 | 27.8 | 23.3 | 50.2 | 83.2 | 103.1 | 75.3 |
| Dcase_NNB | 52.5 | 51.1 | 46.3 | 42.1 | 79.7 | 104.9 | 63.3 | 70.9 |
| Dcase_NNN | 46.1 | 45.9 | 40.9 | 33.8 | 82.1 | 105.4 | 121.6 | 88.8 |

Table 6.15 Statistical summaries of the strain records from the RSGs

| Case | I. Max. response (m strain) max(e) | | | | II. Standard deviation (m strain) std(e) | | | |
|-----------|--|-------|-------|-------|--|-------|-------|------|
| | RSG1 | RSG2 | RSG3 | RSG4 | RSG1 | RSG2 | RSG3 | RSG4 |
| AAA | 166.4 | 144.9 | 121.3 | 96.2 | 36.6 | 33.5 | 27.5 | 21.1 |
| Dcase_BAA | 185.4 | 156.3 | 129.1 | 103.9 | 45.4 | 41.5 | 33.8 | 25.3 |
| Dcase_NAA | 236.7 | 196.3 | 152.0 | 112.6 | 73.8 | 57.1 | 47.8 | 34.0 |
| Dcase_ABA | 192.3 | 169.1 | 116.0 | 113.7 | 48.9 | 45.5 | 31.1 | 27.2 |
| Dcase_ANA | 214.7 | 235.9 | 139.4 | 123.9 | 63.5 | 73.7 | 39.9 | 33.6 |
| Dcase_AAB | 188.6 | 167.6 | 121.9 | 107.8 | 45.7 | 43.1 | 32.5 | 25.5 |
| Dcase_AAN | 203.1 | 167.2 | 169.0 | 112.8 | 49.4 | 46.3 | 46.5 | 26.7 |
| Dcase_BBA | 210.1 | 179.5 | 137.6 | 117.6 | 56.9 | 49.6 | 37.5 | 27.3 |
| Dcase_BNA | 210.9 | 232.8 | 164.2 | 119.6 | 64.9 | 75.2 | 46.4 | 33.9 |
| Dcase_NBA | 246.4 | 215.3 | 175.2 | 131.8 | 83.5 | 69.5 | 52.5 | 37.1 |
| Dcase_NNA | 266.8 | 273.6 | 188.8 | 136.9 | 119.3 | 114.7 | 73.4 | 50.6 |
| Dcase_BAB | 213.6 | 184.3 | 135.4 | 105.5 | 58.1 | 50.1 | 36.8 | 28.7 |
| Dcase_BAN | 240.7 | 188.6 | 194.1 | 123.8 | 60.1 | 52.0 | 51.9 | 30.3 |
| Dcase_NAB | 266.3 | 221.2 | 165.4 | 137.5 | 86.7 | 70.9 | 51.1 | 37.6 |
| Dcase_NAN | 278.4 | 221.1 | 201.9 | 134.5 | 89.4 | 72.6 | 72.0 | 40.5 |
| Dcase_ABB | 195.7 | 171.4 | 128.2 | 102.9 | 52.3 | 48.8 | 36.9 | 28.7 |
| Dcase_ABN | 210.7 | 186.2 | 171.5 | 105.8 | 55.7 | 52.2 | 53.1 | 30.6 |
| Dcase_ANB | 222.9 | 240.5 | 151.1 | 131.8 | 68.6 | 79.4 | 47.9 | 36.1 |
| Dcase_ANN | 225.4 | 243.4 | 212.1 | 129.0 | 73.9 | 85.1 | 69.5 | 38.4 |
| Dcase_BBB | 223.6 | 191.6 | 148.2 | 114.6 | 63.3 | 55.1 | 40.8 | 30.6 |
| Dcase_BBN | 253.7 | 205.6 | 208.3 | 129.7 | 68.7 | 59.3 | 58.2 | 33.9 |
| Dcase_NBB | 302.4 | 234.4 | 186.6 | 145.6 | 121.5 | 94.7 | 72.5 | 52.8 |
| Dcase_BNN | 255.0 | 260.0 | 244.2 | 147.9 | 96.7 | 99.8 | 81.0 | 45.0 |
| Dcase_NNB | 298.8 | 300.9 | 207.0 | 148.0 | 162.8 | 158.3 | 92.3 | 67.6 |
| Dcase_NNN | 307.1 | 302.7 | 273.2 | 171.8 | 173.4 | 170.7 | 134.2 | 72.6 |

Table 6.15 (Continue)

| Case | III. $\frac{\text{std}(\mathbf{e})}{\text{max}(\mathbf{e})}$ (%) | | | | IV. $\Delta \text{max}(\mathbf{e}) / \text{baseline}$ (%) | | | |
|-----------|--|------|------|------|---|-------|-------|------|
| | RSG1 | RSG2 | RSG3 | RSG4 | RSG1 | RSG2 | RSG3 | RSG4 |
| AAA | 22.0 | 23.1 | 22.7 | 21.9 | / | / | / | / |
| Dcase_BAA | 24.5 | 26.5 | 26.2 | 24.4 | 11.4 | 7.9 | 6.4 | 8.0 |
| Dcase_NAA | 31.2 | 29.1 | 31.4 | 30.2 | 42.3 | 35.5 | 25.4 | 17.0 |
| Dcase_ABA | 25.4 | 26.9 | 26.8 | 23.9 | 15.6 | 16.7 | -4.3 | 18.3 |
| Dcase_ANA | 29.6 | 31.2 | 28.6 | 27.1 | 29.1 | 62.8 | 15.0 | 28.9 |
| Dcase_AAB | 24.2 | 25.7 | 26.6 | 23.6 | 13.4 | 15.7 | 0.6 | 12.1 |
| Dcase_AAN | 24.3 | 27.7 | 27.5 | 23.7 | 22.1 | 15.4 | 39.3 | 17.3 |
| Dcase_BBA | 27.1 | 27.6 | 27.3 | 23.2 | 26.3 | 23.9 | 13.5 | 22.3 |
| Dcase_BNA | 30.8 | 32.3 | 28.3 | 28.4 | 26.8 | 60.7 | 35.4 | 24.4 |
| Dcase_NBA | 33.9 | 32.3 | 30.0 | 28.1 | 48.1 | 48.6 | 44.5 | 37.1 |
| Dcase_NNA | 44.7 | 41.9 | 38.9 | 37.0 | 60.4 | 88.9 | 55.7 | 42.4 |
| Dcase_BAB | 27.2 | 27.2 | 27.2 | 27.2 | 28.4 | 27.2 | 11.7 | 9.7 |
| Dcase_BAN | 25.0 | 27.6 | 26.7 | 24.5 | 44.7 | 30.2 | 60.1 | 28.8 |
| Dcase_NAB | 32.5 | 32.0 | 30.9 | 27.3 | 60.0 | 52.7 | 36.4 | 43.0 |
| Dcase_NAN | 32.1 | 32.9 | 35.7 | 30.1 | 67.3 | 52.6 | 66.5 | 39.8 |
| Dcase_ABB | 26.7 | 28.5 | 28.8 | 27.9 | 17.7 | 18.3 | 5.7 | 7.0 |
| Dcase_ABN | 26.4 | 28.1 | 31.0 | 28.9 | 26.7 | 28.5 | 41.4 | 10.0 |
| Dcase_ANB | 30.8 | 33.0 | 31.7 | 27.4 | 34.0 | 66.0 | 24.6 | 37.0 |
| Dcase_ANN | 32.8 | 35.0 | 32.8 | 29.8 | 35.5 | 68.0 | 74.9 | 34.2 |
| Dcase_BBB | 28.3 | 28.7 | 27.5 | 26.7 | 34.4 | 32.3 | 22.2 | 19.2 |
| Dcase_BBN | 27.1 | 28.8 | 27.9 | 26.1 | 52.5 | 41.9 | 71.8 | 34.8 |
| Dcase_NBB | 40.2 | 40.4 | 38.8 | 36.3 | 81.8 | 61.8 | 53.9 | 51.4 |
| Dcase_BNN | 37.9 | 38.4 | 33.2 | 30.4 | 53.3 | 79.5 | 101.4 | 53.8 |
| Dcase_NNB | 54.5 | 52.6 | 44.6 | 45.7 | 79.6 | 107.7 | 70.7 | 53.8 |
| Dcase_NNN | 56.5 | 56.4 | 49.1 | 42.3 | 84.6 | 108.9 | 125.3 | 78.6 |

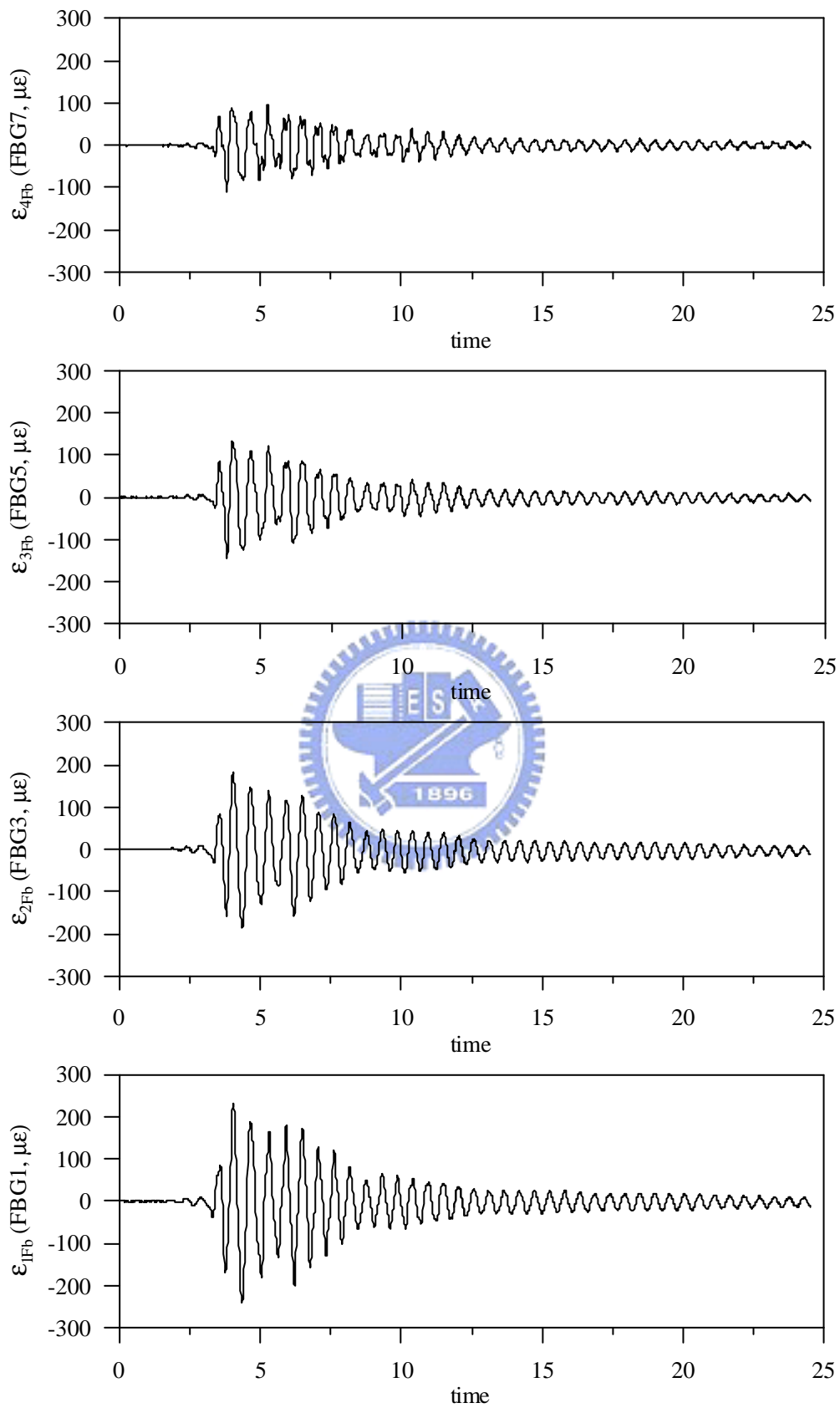


Figure 6.32 Strain time-history responses of the FBG sensors at BW for AAA

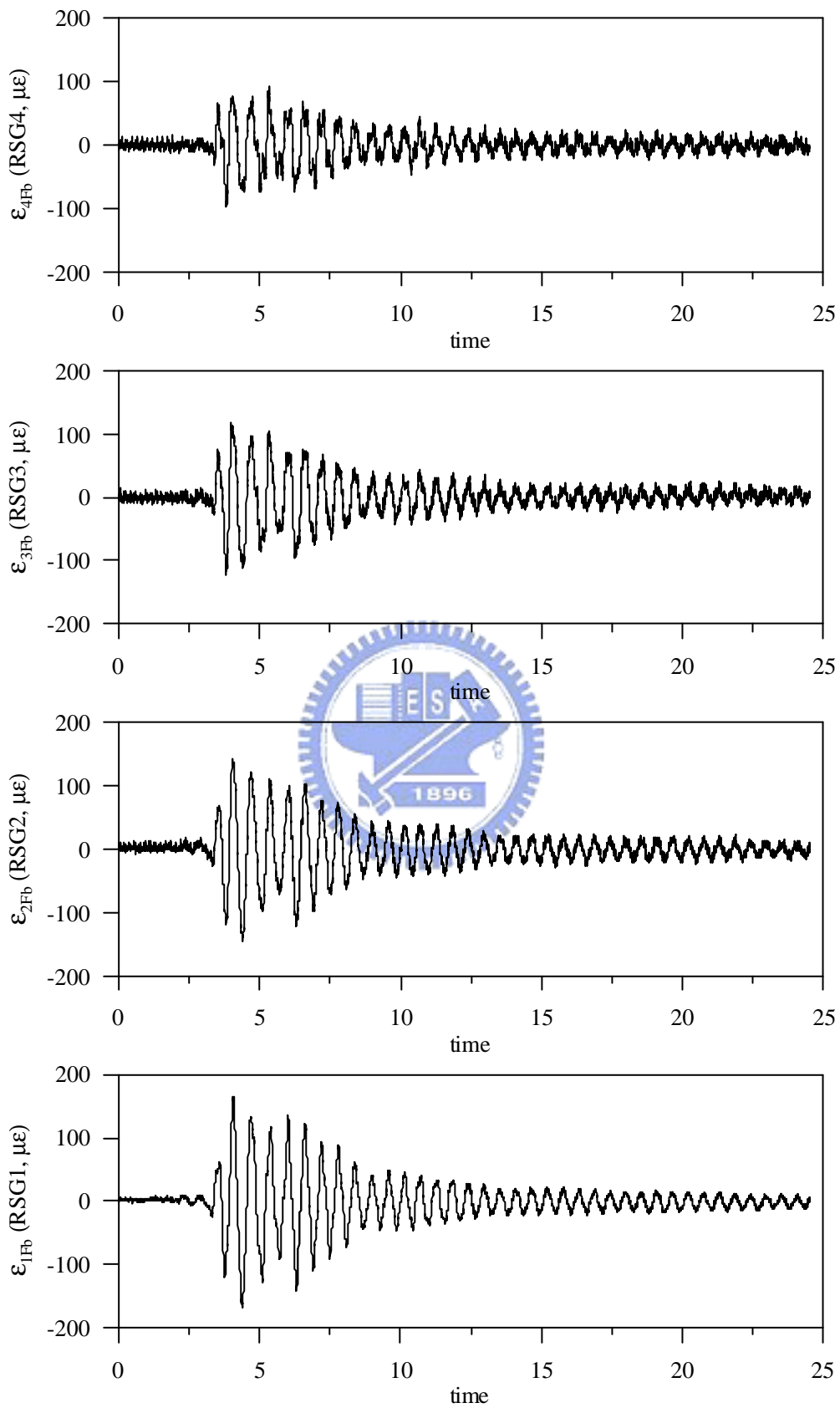


Figure 6.33 Strain time-history responses of the RSGs at BW for AAA

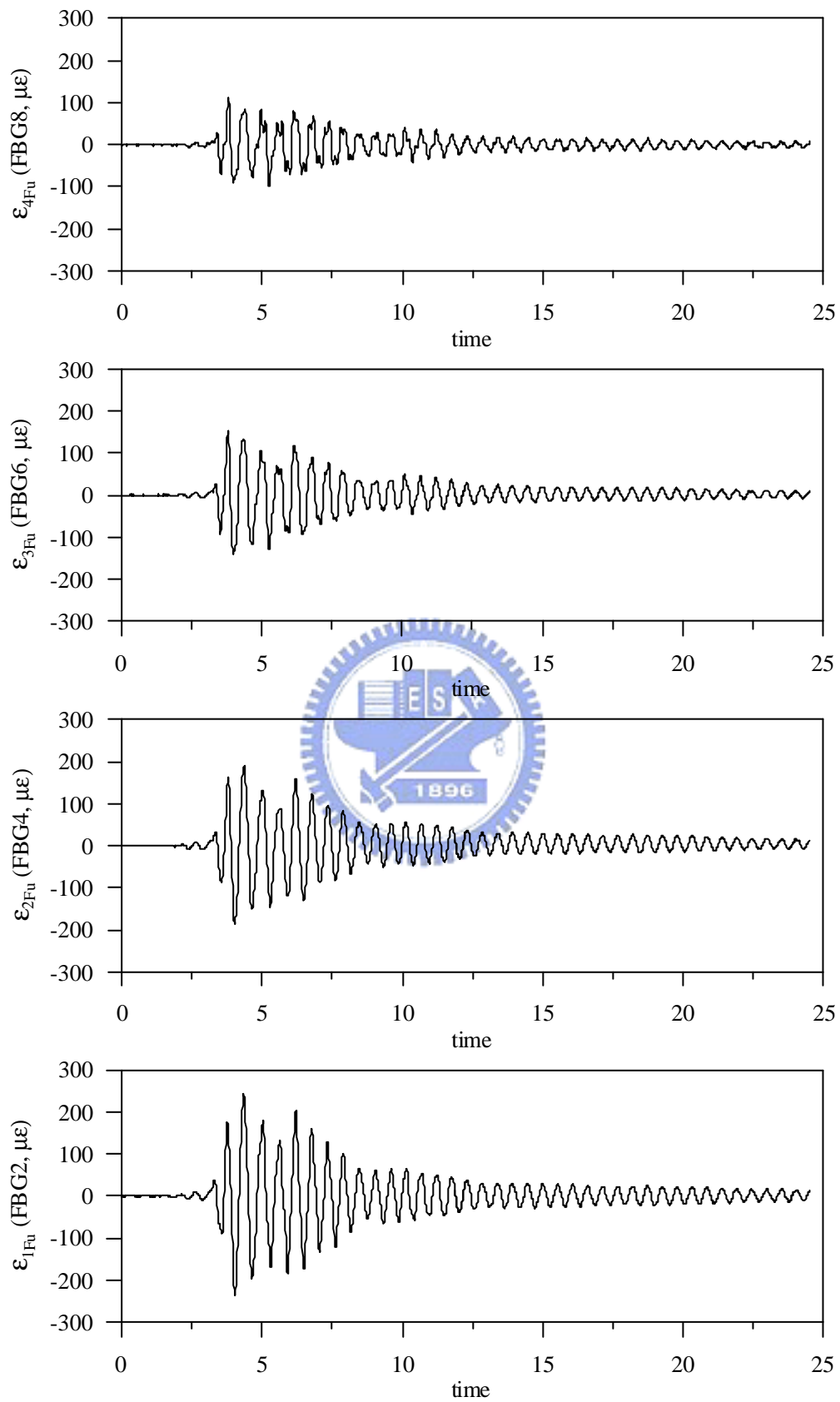


Figure 6.34 Strain time-history responses of the FBG sensors at TE for AAA

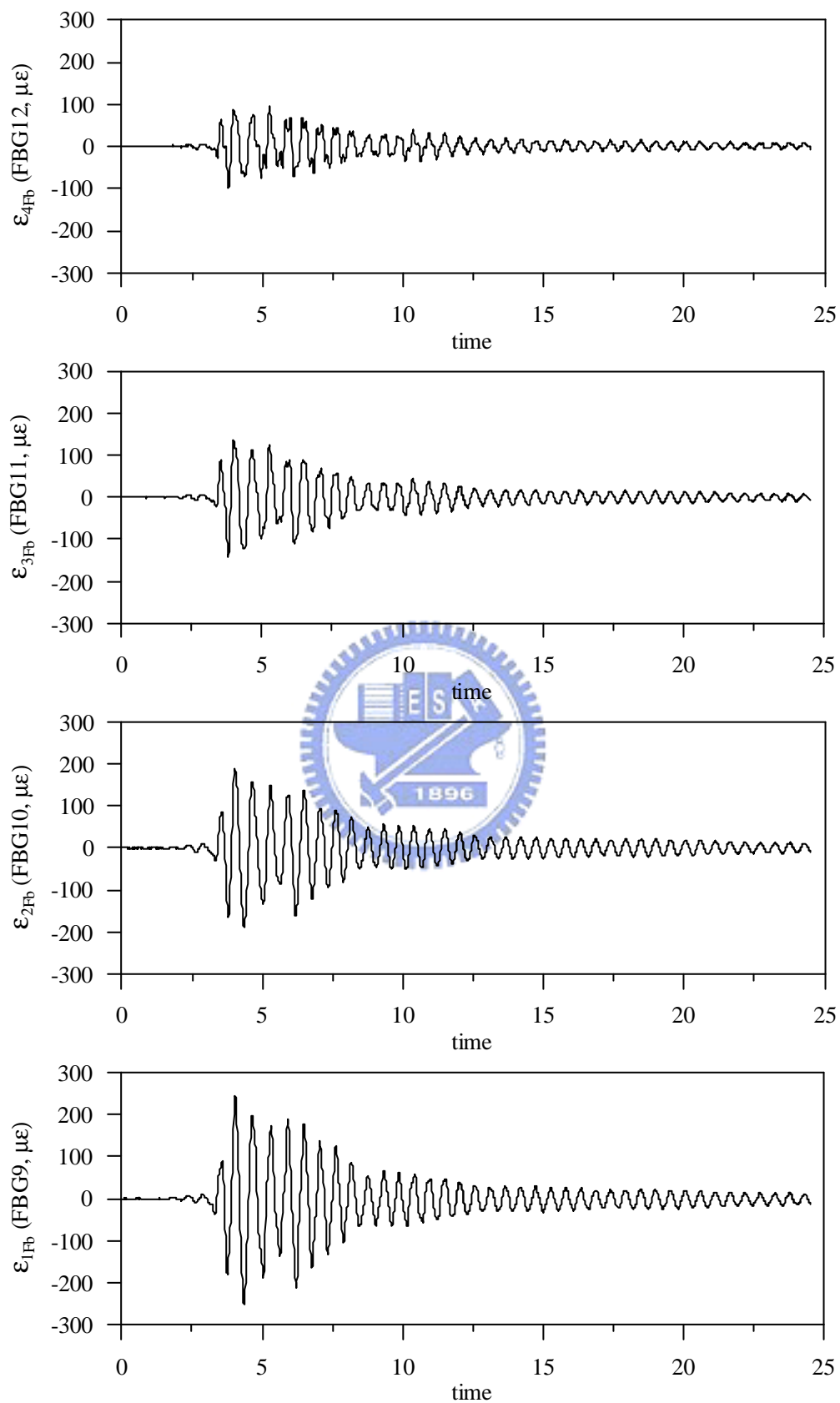


Figure 6.35 Strain time-history responses of the FBG sensors at BW for AAA